Ulrich Stopper, Wolfgang Meier, Rajesh Sadanandan, Michael Stöhr, Manfred Aigner, Ghenadie Bulat, Experimental Study of Industrial Gas Turbine Flames Including Quantification of Pressure Influence on Flow Field, Fuel/Air Premixing and Flame Shape, Combust. Flame 160(2013), 2103-2118.

The original publication is available at www.elsevier.com

http://dx.doi.org/10.1016/j.combustflame.2013.04.005

Experimental Study of Industrial Gas Turbine Flames Including Quantification of Pressure Influence on Flow Field, Fuel/Air Premixing and Flame Shape

Ulrich Stopper[a], Wolfgang Meier[a]*, Rajesh Sadanandan[a], Michael Stöhr[a], Manfred Aigner[a], Ghenadie Bulat[b]

[a] Institut für Verbrennungstechnik, Deutsches Zentrum für Luft- und Raumfahrt (DLR), Pfaffenwaldring 38,
D-70569 Stuttgart, Germany

[b] Siemens Industrial Turbomachinery Ltd., PO Box 1, Waterside South, Lincoln, LN5 7FD, England, UK

*Corresponding author: wolfgang.meier@dlr.de

Abstract

A commercial swirl burner for industrial gas turbine combustors was equipped with an optically accessible combustion chamber and installed in a high-pressure test-rig. Several premixed natural gas/air flames at pressures between 3 and 6 bar and thermal powers of up to 1 MW were studied by using a variety of measurement techniques. These include particle image velocimetry (PIV) for the investigation of the flow field, one-dimensional laser Raman scattering for the determination of the joint probability density functions of major species concentrations, mixture fraction and temperature, planar laser induced fluorescence (PLIF) of OH for the visualization of the flame front, chemiluminescence measurements of OH* for determining the lift-off height and size of the flame and acoustic recordings. The results give insights into important flame properties like the flow field structure, the premixing quality and the turbulence-flame interaction as well as their dependency on operating parameters like pressure, inflow velocity and equivalence ratio. The 1D Raman measurements yielded information about the gradients and variation of the mixture fraction and the quality of the fuel/air mixing, as well as the reaction progress. The OH PLIF images showed that the flame was located between the inflow of fresh gas and the recirculated combustion products. The flame front structures varied significantly with Reynolds number from wrinkled flame fronts to fragmented and strongly corrugated flame fronts. All results are combined in one database that can be used for the validation of numerical simulations.

Keywords

high pressure combustion
gas turbine combustor
turbulent premixed swirl flame
Raman scattering
particle image velocimetry
turbulence-chemistry interaction

1. Introduction

The understanding of combustion in gas turbines (GTs) has been strongly improved by the combined and mutually supporting effort of experimental studies in GT model combustors and numerical simulations using advanced methods like Large Eddy Simulation (LES) [1,2]. In particular, GT model combustors with optically accessible combustion chambers which facilitate the application of laser and optical measurement techniques enabled a deeper insight into the complex interaction between flow field, combustion and acoustic modes of the system. Among the main advantages of these techniques

is their ability to non-intrusively measure instantaneous two-dimensional distributions of various quantities, to image short-lived combustion radicals and heat release rates, to measure several quantities simultaneously and to capture the temporal development using high-speed imaging techniques [3-6]. Main research topics in GT combustion have been thermo-acoustic instabilities, coherent flow structures, flame stabilization, pollutant emissions, effects of mixing and turbulence-chemistry interaction, fuel flexibility, flashback and the potential of new combustion systems. Many laser-based studies in GT (model) combustors addressed these topics, for example, the dynamics of swirl flames by using particle image velocimetry (PIV) for the characterization of the flow field or planar laser-induced fluorescence (PLIF) for the measurement of the flame front, often in combination with chemiluminescence imaging [7-11]. PLIF was also applied to investigate the mechanisms of flame stabilization [12-14]. The role of equivalence ratio fluctuations and effects of unmixedness in lean premixed flames were investigated by Schürmans et al. [15] using chemiluminescence and infrared absorption measurements and by Meier et al. [16] using laser Raman scattering. Further examples of similar studies are given in the tables of the papers by Palis et al. [17] and Dhanuka et al. [18].

The cited investigations and some more have been performed at atmospheric pressure. At elevated pressure, the experimental complexity and costs increase drastically. In high-pressure test-rigs optical access is limited, laser and signal beams must pass through several windows (pressure housing and combustion chamber), windows degrade from the high heat load to the glass surface and the pressure broadening of spectral lines often leads to signal decrease. Thus, fewer studies using optical and laser based techniques have been reported at high-pressure GT conditions. However, such investigations are important because increased pressure changes the physical and chemical quantities in the flame, like Reynolds number, viscosity, reaction rate related quantities like flame speed, ignition delay time or pollutant formation and, in general, all effects of turbulence-chemistry interaction. For example, Griebel et al. measured the influence of pressure and turbulence on the flame speed of premixed turbulent flames [19], Lückerath et al. studied flame stabilization in a staged GT model combustor [20], Strakey et al. and Fleck et al. investigated the impact of hydrogen in GT combustors [21,22], the role of coherent structures was studied by Janus et al. [23], mixing and reaction progress by Ax et al. [24] and new burner concepts were investigated with coherent anti-Stokes Raman spectroscopy (CARS) by Lammel et al. [25] and Thariyan et al. [26].

One of the targets of the experimental studies was the generation of validation data for numerical simulations. Here, significant improvements for the prediction of GT combustion have been achieved with Large Eddy Simulation (LES) [27-38]. LES is a powerful and promising modeling technique particularly for highly swirling and unsteady flows. For gas turbine combustion chambers, particular attention is given to development of the flow field, coherent structures, flame front and thermo-acoustic instabilities. In studies of industrial geometries, [27,29,30,39,40], the LES formulation was completed considering reduced chemistry (2-, or 3-step). Good agreement was generally obtained for the velocity and scalar fields with over-prediction of temperature and species in most cases. The use of reduced chemistry did not exploit the full potential of the LES method to capture the turbulence and chemistry interaction of industrial flows. The major objective of industrial LES studies appears to aim at capturing more turbulent features, rather than additional chemistry. This was most likely dictated by the lack of detailed experimental data for the species composition.

This paper presents results from optical and laser-based measurements performed in an optically accessible combustion chamber equipped with an original Siemens Industrial Turbomachinery, Lincoln dry low emissions (SITL DLE) combustor. The burner and combustion chamber were installed in the high-pressure test rig HBK-S at DLR in Stuttgart and operated with natural gas and preheated air at pressures up to 6 bar. Particle image velocimetry (PIV) was applied to measure the flow field, 1D laser Raman scattering for the simultaneous determination of the major species concentrations, mixture fraction and temperature, PLIF of OH and chemiluminescence imaging for the visualization of flame structures, as well as chemical analysis of the exhaust gas composition. A particular challenge was the application of single shot 1D laser Raman scattering under GT conditions in flames with thermal powers of up to 1 MW. With this technique, it was for the first time possible to quantify spatial mixture fraction gradients and effects of unmixedness in an industrial GT combustor

under realistic operating conditions. The combustion parameters that were varied within the investigations were the pressure in the combustion chamber, pressure drop at the burner (and thus flow velocity) and the equivalence ratio. A comparable data set from a high-pressure GT flame comprising flow velocities, flame structures and joint probability density functions of major species concentrations, temperature and mixture fraction has not been documented before. The main goals of the measurements were a better understanding of the mixing and reaction progress, flow field structures and unsteady combustion processes as well as the establishment of a comprehensive experimental database for the validation of numerical simulations. It is envisioned that this database may serve as a ”standard” test case for the comparison of the performance of different computational fluid dynamic (CFD) codes.

2. Experimental setup and measurement techniques

2.1. Burner, combustor and test rig

The studied burner was an original-sized industrial GT burner from Siemens. It is the smallest commercial version of the company’s DLE combustor family which is installed in the small and medium sized turbo-machines SGT-100 to 400 as a retrofit solution [41] and as the standard equipment in the current product line [42,43]. The fields of application of these engines cover both the production of electrical and mechanical power in a range between 4.9 and 15 MW. The burner is built up of a radial swirler with twelve rectangular channels (see Fig. 1). Each channel has multiple small holes for the injection of fuel that mixes with the air flow. Downstream of the swirler the air-fuel mixture flows through a ~46 mm long tube in which the largest part of the premixing takes place. The exit diameter of this ”burner nozzle” is 86 mm. The pilot burner is only used for part load operation in the commercial gas turbine [44]. In the present work, it was used for the flame ignition and switched off after the startup procedure. The development of the DLE combustion system in Lincoln started in the mid-nineties [45,46]. It aims for a fast mixing of fuel and air prior to the combustion in order to generate a uniform flame temperature distribution and hence low NO_x emissions [47-49]. Experimental [50,51] as well as numerical studies [52] were performed to analyze such emissions and to validate a novel NO_x prediction method [53]. Further experimental work was focused on finding correlations between acoustic oscillations and the flame behavior [54] as well as the wall heat transfer [55]. In recent experiments the DLE combustor has also been used for testing a novel stereoscopic high-speed imaging system [56,57]. The burner has a dual fuel capability (gaseous/liquid fuel), and probe measurements of temperature, species distributions and emissions have been undertaken with conventional diesel [58] and biodiesel [59] as fuel. No liquid fuel was used in the study presented here. CFD simulations of the isothermal and the reacting flow in the DLE combustor have also been performed. Some of them were based on Reynolds-averaged Navier-Stokes (RANS) calculations [60,61] whereas in the more recent studies LES was used and different turbulence and combustion models were validated [62-64].

For the experiments presented here, the DLE burner (pilot and swirler assemblies, see Fig. 1) was attached to a generic combustion chamber with dimensions similar to the single SGT-100 combustor can. For an optical access, the side walls of the combustion chamber consisted of large windows, which is why the cross-section of the combustion chamber had to be square instead of circular. The windows (held by water-cooled posts) were built up of two parallel quartz glass plates and the gap between them was used for cooling by the air flow that afterwards entered the radial swirler and took part in the combustion. The circular burner nozzle was surrounded by a metallic burner panel equipped with impingement cooling. After the contact with this burner panel, the cooling air (about 8.8 % of the total air mass flow that took part in the combustion) entered the combustion chamber at the square outer rim of the panel. A water-cooled exhaust gas transition duct served as an adaptor between the combustion chamber (width 165 mm) and the exhaust pipe (circular cross-section, diameter: 50 mm). The whole combustor was installed at the high-pressure test rig facility (HBK-S) at the German Aerospace Center (DLR) in Stuttgart. The optical access of the pressure vessel surrounding the combustion chamber consisted of four thick quartz glass windows. The air was electrically preheated to 400 °C. The used fuel was natural gas (average mole fractions: 96.6 % CH_4, 1.66 % C_2H_6, 0.36 %

C_3H_8, 0.05 % n-C_4H_{10}, 0.05 % iso-C_4H_{10}, 0.41 % CO_2, 0.90 % N_2). The air mass flow was deduced from the measured pressure drop over a calibrated flow aperture and the air temperature measured by a thermocouple. The fuel mass flow was measured by a Coriolis flow meter. The accuracies of the mass flows were estimated to approximately ±4% for the air flow and ±3% for the natural gas flow.

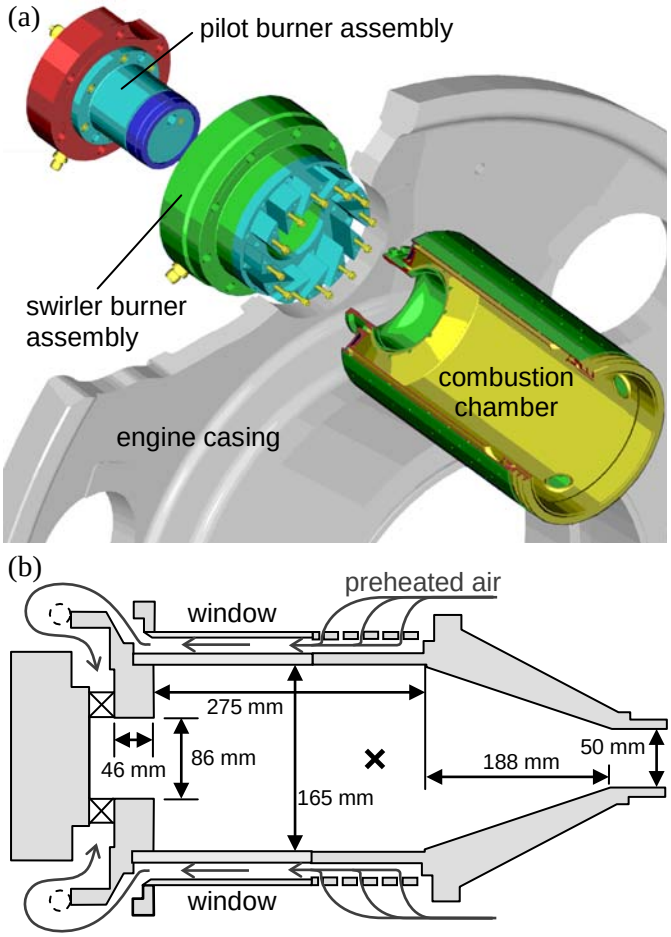

Fig. 1. The industrial burner with the commercial cylindrical combustion chamber (a) and with the optically accessible combustion chamber (b) (based on [65]). A cross marks the location of the acoustic probe. Two dashed circles represent the perforated ring tube used for particle seeding.

2.2. Measurement techniques

Only the most important specifications about the experimental setups are given here. More detailed descriptions with figures of the optical and laser-optical setups are published in earlier articles [65,66]. All image processing steps were performed with the Software DaVis (LaVision GmbH).

2.2.1. Flow velocity measurements with particle image velocimetry (PIV)

A commercially available PIV system was used (LaVision FlowMaster). The air flow was seeded with TiO_2 particles with a diameter of 1 µm. The particles were injected a few centimeters upstream of the swirler through a perforated ring tube (see Fig. 1). A laser sheet was generated from the output of a frequency-doubled Nd:YAG laser (New Wave Solo PIV 120, λ = 532 nm) by sheet forming optics. This 1 mm thick laser sheet was oriented vertically and located within the symmetry plane of the combustion chamber. For the measurement of the instantaneous flow field, the particles were illuminated with a double pulse. Each pulse had a duration of 5 ns and an energy of 120 mJ. The time interval between the pulses of a pulse pair was 10 – 15 µs. The corresponding pair of particle

distributions was recorded with a CCD camera (LaVision Imager Intense, 1376 × 1024 pixels) equipped with a lens of 50 mm focal length with an aperture setting of *f*/5.6 and a narrow band interference filter for λ = 532 nm. The repetition rate of the PIV measurements was 5 Hz. In the analysis circular interrogation windows with a diameter of 1.67 mm were used. Because of relatively good experimental conditions in the operating case A (see table 2), the diameter was reduced to 1.1 mm in this case.
The typical statistical error for the vector lengths in the ensemble averaged flow field is 0.93 m/s. This is a relative statistical error of less than 5 % in the inflow zone. The accuracy of the measured instantaneous flow velocities has a theoretical limit of ~ 0.7 m/s, assuming a resolution of 0.1 pixels in the localization of the cross-correlation peak. This systematic error is further increased by experimental influences that are difficult to quantify because they depend on the seeding particle density, the window transparency, the turbulence of the flow and the aperture ratio of the detection optics.

An additional systematic deviation is caused by the perspective error in two-component PIV experiments [67]. This error increases from the center of the field of view towards its outer parts. It depends on the out-of-plane component of the flow velocity. As this component was not measured, the perspective error cannot be quantified. It is assumed to be negligibly small, because the effect was minimized by using a PIV camera lens with a long focal length.

2.2.2. Species and temperature measurements with 1D laser Raman spectroscopy
A laser system built up of three double-resonator Nd:YAG lasers (Spectra Physics PIV-400) was used. The system produces a train of six single pulses (single pulse length: 7 ns, delay: 50 ns) that is frequency-doubled to λ = 532 nm and irradiated into a pulse stretching unit consisting of several mirrors and beam splitters, in order to reduce the peak power of the pulse train from ~45 MW to a value lower than ~9 MW without losing large amounts of total energy [68]. The nominal system output was 1.2 J within 350 ns. However, the system output during the experiment was 1 J within 300 ns, as one resonator was not working. All these components were integrated in two containers to provide mobility, laser safety, temperature stability, vibration damping and an easy control of the leveling of the system.

The setup was the same as described previously [65]. The laser beam was guided vertically through the combustor with the focus always being located in the horizontal symmetry plane. Applying astigmatic focusing optics, a focus with a stretched shape was produced. An 8 mm long central beam section of the focus was imaged onto the entrance slit of a grating spectrograph (Acton-Research SpectraPro 300i, type: Czerny-Turner, f = 300 mm with aperture *f*/4.2, grating: 490.4 lines per mm) by an apochromatic lens system (Linos, f = 230 mm, aperture *f*/1.5) that was protected with an actively cooled IR filter (Schott KG2). The output of the spectrograph was recorded with an intensified CCD camera of Princeton Instruments. The CCD chip had 1340 × 1300 pixels with 16 bit/pixel in the A/D conversion. For noise reduction, it was cooled to -20 °C. The Gen III HQ image intensifier was equipped with a P43 phosphor and fiber coupling optics. Raw images showed a spectrum in the horizontal direction (λ = 547 – 711 nm, resolution: ~3 nm) and the 1D spatial distribution along the laser beam in the vertical direction. With a hardware binning, the chip resolution was reduced to 268 × 28 super pixels leading to a much smaller readout noise. Depicting the central beam section of 8 mm onto 28 super pixel rows resulted in 28 observation volumes that were investigated simultaneously. In a rough approximation, each observation volume can be seen as a cylinder with a diameter of ~0.6 mm and a height of 0.29 mm (see Fig. 2). The repetition rate of the Raman single shot measurements was 10 Hz. Several measurement locations in the horizontal symmetry plane of the combustor were scanned by moving the laser guide, focusing and detection optics with a 2D translation stage. At each *x*-*y* location 500 single shots were recorded. Each single shot contains an instantaneous profile of 28 observation volumes spanning over a vertical line of 8 mm. The *x*-*y* locations were chosen in a way that radial and axial horizontal profiles can be produced from the ensemble averaged results.

The software that was used for the analysis has been developed at DLR Stuttgart. It divides the recorded spectra into separate channels of which each represents one species. The channel intensities

were corrected for background signal, laser pulse energy and channel cross-talk (due to overlapping Raman bands). The temperature-dependent spectral shift and broadening of the Raman bands were taken into account via calibration measurements that were performed at an electrical gas heater as well as in premixed flat laminar CH_4/air and H_2/air flames of known temperature and composition stabilized on a matrix burner. The exhaust gas temperatures of the laminar flames were measured before the Raman experiments by CARS with an accuracy of 2.5 - 3%. The exhaust gas composition was determined from the mass flow rates using equilibrium calculations for the measured temperatures with the software GasEq [69]. For the calibration measurements, the GT burner was replaced by the gas heater or the matrix burner and an identical optical setup as for the measurements in the GT flames was used. This ensured the comparability of the results from the calibration and GT burner measurements. However, calibration measurements were performed at atmospheric pressure and the conversion to the pressure of the GT flames was done in the data evaluation procedure.

From the intensity ratios between the distinct Raman bands measured in the GT flames the mole fractions of the major species (CO_2, O_2, N_2, C_xH_y, H_2O) were deduced. The overall intensity of the spectrum in combination with the absolute pressure measured by a probe provided information about the total species number density and temperature in the observation volume. During the experiments, the transmissivity of the quartz windows which were exposed to the flame degraded. Due to the temporally and spatially varying window transmissivity, an absolute temperature calibration of the system was sometimes not possible. For example, the determination of the temperature usually requires a normalization of the Raman signals by the laser pulse energy at the measuring location, which was hardly possible with degraded windows. Therefore, the temperatures were determined by comparing the Raman signal from a sample with unknown temperature with that from a sample containing a fresh fuel/air mixture (without any combustion products present). The temperatures of the air and fuel were measured by thermocouples before entering the burner. In case that fresh fuel/air mixtures were never present at a measuring location, the temperature of completely reacted mixtures were used for comparison. These temperatures were taken as the adiabatic flame temperature for the measured mixture composition [69]. The corresponding “calibration factors” were not determined on a single-shot basis but from conditionally averaged mean values in an iterative procedure. It is pointed out, that the determination of the species mole fractions was hardly affected by the temperature calibration procedure because they were determined from the relative signal strength. Additional processing steps, like statistical evaluations, were done with the software Origin (OriginLab Co.).

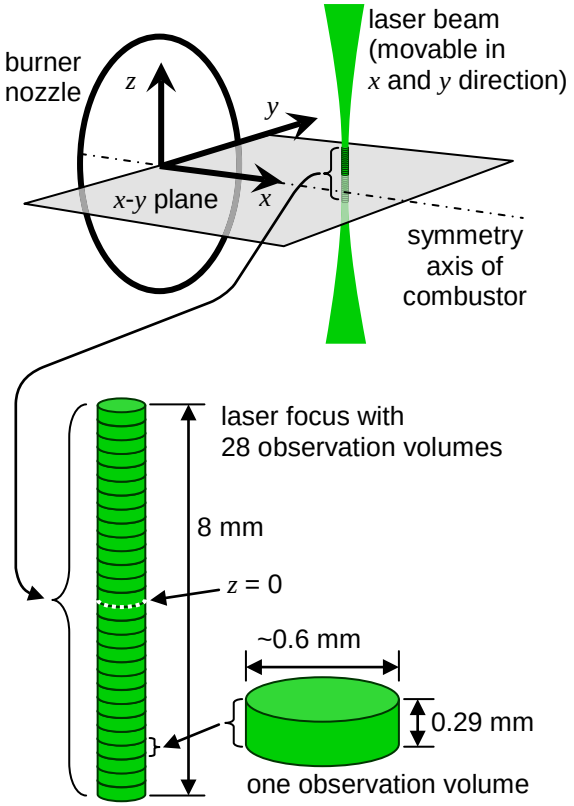

Fig. 2. In the Raman experiment the focal region of the laser beam was divided into 28 simultaneously observed volumes spanning over a length of 8 mm.

Table 1 lists the typical values for the statistical error of the single shots, the systematic error and the total error of the single shots in the results of the Raman measurements. The latter is defined as the square root of the sum of the statistical and the systematic errors squared. The calculation takes into account both shot-to-shot variations and variations between the single observation volumes in one single shot. For each of the three errors, two values, one for the unburned reactants and one for the hot products, have been estimated, because of the different chemical composition and the inverse proportionality between the signal/noise ratio and the gas density. The errors strongly depend on the experimental conditions like the window transparency, which is why the given values have to be regarded as mean values for all measurement series. Some of the measurement results (especially at the cases A and C, see table 2) have errors that are only half as large as these typical values.

It is noted that the precision of single-shot Raman measurements depends primarily on the number of detected Raman scattered photons which in turn is proportional to the size of the measurement volume. In the present study the segments along the laser line were chosen to have a length of 0.29 mm. A binning of 2 segments would, for example, improve the precision by a factor of $2^{1/2}$ at the cost of spatial resolution. The data set allows for a binning in a post processing step in order to reduce the measurement error.

Table 1
Statistical, systematic and total errors of the Raman measurement in a single observation volume of a single shot. The values are estimates for measurements with a medium quality.

	unburned preheated fuel/air mixture ($T \approx 640$ K):						
	$\frac{\Delta T}{T}$	ΔX_{CO_2}	$\frac{\Delta X_{O_2}}{X_{O_2}}$	$\frac{\Delta X_{N_2}}{X_{N_2}}$	$\frac{\Delta X_{NG}}{X_{NG}}$	ΔX_{H_2O}	Δf
precision	5 %	0.3 vol.-%	5 %	2 %	2 %	0.3 vol.-%	0.0068
accuracy	3 %	0.2 vol.-%	3 %	4 %	4 %	0.2 vol.-%	0.0014
total error	6 %	0.4 vol.-%	6 %	4 %	4 %	0.3 vol.-%	0.0069

	fully reacted hot products ($T \approx 1700$ K – 1900 K):						
	$\frac{\Delta T}{T}$	$\frac{\Delta X_{CO_2}}{X_{CO_2}}$	$\frac{\Delta X_{O_2}}{X_{O_2}}$	$\frac{\Delta X_{N_2}}{X_{N_2}}$	$\Delta X_{C_xH_y}$	$\frac{\Delta X_{H_2O}}{X_{H_2O}}$	Δf
precision	10 %	17 %	17 %	2 %	0.2 vol.-%	11 %	0.0041
accuracy	4 %	12 %	13 %	6 %	0.3 vol.-%	6 %	0.0031
total error	10 %	20 %	21 %	6 %	0.4 vol.-%	13 %	0.0051

2.2.3. Flame shape measurements with OH chemiluminescence*

An ICCD camera (Princeton Instruments PI-Max, 512 × 512 pixels with 16 bit/pixel) was equipped with an achromatic UV lens (f = 100 mm, $f/2$) and a band pass filter (λ = 300 – 325 nm) with high transmittance for the light emitted by the spontaneous relaxation ($^2\Sigma^+ \rightarrow {}^2\Pi$) of electronically excited hydroxyl radicals (OH*). The camera was run with an exposure time of 40 µs at a repetition rate of 3 Hz.

2.2.4. OH and flame front mapping with planar laser induced fluorescence (PLIF) of OH

The same detection system as in the chemiluminescence measurements was applied but with an UV laser for the excitation of OH radicals. A frequency-doubled dye laser Lumonics HD-500 with a pulse length of 8 ns and a pulse energy of 4.6 – 5.5 mJ was used. It was pumped by a Nd:YAG laser Quanta Ray DCR-2. The laser output was tuned to the absorption line Q_1 (J = 8, v = 1 ← v = 0) of the $^2\Sigma^+ \leftarrow {}^2\Pi$ transition at λ = 283.5 nm. The exposure time was 400 ns, and the repetition rate was 3 Hz.

2.2.5. Acoustic measurements

The end of a 1.3 m long steel tube (inner diameter: 4 mm) was located at the position that is marked with a cross in Fig. 1. At the other end a piezo acoustic microphone (Kistler) was installed that recorded the pressure oscillations inside the combustion chamber at a high sampling rate. As the effect of the steel tube on the calibration of the microphone was not investigated and only one acoustic probe at one measurement location was used, the measured results can only serve as a rough indicator for the real pressure oscillations inside the combustion chamber. The acoustic data was processed with the Software Matlab (MathWorks, Inc.). The processing included FFT filtering, subtraction of the mean signal value and the identification of the acoustic phase at a given point in time, e. g. the laser trigger.

2.3. Operating conditions

Table 2 lists the most important operating conditions that were investigated. Other operating points have been measured but are not included here because they are beyond the scope of this paper. p is the pressure inside the combustion chamber, T_{air} is the air temperature measured at the swirler inlet, $\dot{m}_{air}$ is the air mass flow rate including the cooling air for the burner panel, $\dot{m}_{fuel}$ is the mass flow rate of natural gas and u_{in} is a rough estimation (based on the volume flow rate and the burner geometry) of the absolute value of the three-component bulk flow velocity in the inflow zone at the exit of the

burner nozzle. λ stands for the air equivalence ratio including the cooling air for the burner panel. The thermal power $P_{th,h}$ was calculated with the higher heating value. The Reynolds number Re_{in} is based on a characteristic length of 23 mm (radial distance between inner wall of burner nozzle and inner shear layer of averaged flow field at exit of burner nozzle), on the viscosity of the inflowing gas mixture and on u_{in}. Case "Iso" was a PIV measurement at an isothermal flow of non-preheated air. The results shown in this paper stem from case Iso and from the three standard flames with the highest results quality, the cases A, B and C.

Table 2
Overview of the most relevant operating conditions included in the database indicating whether PIV, one-dimensional Raman scattering (1DR), OH* chemiluminescence (OH*), OH PLIF (OH) or acoustic measurements (Ac.) were performed (+) or not (–).

case	p [bar]	T_{air} [°C]	$\dot{m}_{air}$ [g/s]	$\dot{m}_{fuel}$ [g/s]	u_{in} [m/s]	λ	$P_{th,h}$ [kW]	Re_{in} /10^3	PIV	1DR	OH*	OH	Ac.
Iso	5	15	251	0	12.9	∞	0	100	+	–	–	–	–
A	3	412	175	6.20	40.6	1.67	335	39	+	+	+	+	+
B	6	404	352	12.5	40.4	1.67	685	78	+	+	+	+	+
C	3	411	304	11.0	69.9	1.66	598	67	+	+	+	+	+
D	6	408	555	19.6	63.3	1.69	1080	120	–	+	+	–	+

2.4. Additional Measurements

Additionally to the techniques described above, other measurements were applied to these standard flames: Conventional RGB video of the flame luminosity in the visible spectral range, analyses of the chemical compositions of natural gas and exhaust gas as well as measurements of the gas temperatures, wall temperatures, absolute pressures and pressure drops. Figure 3 shows an exemplary still image of an RGB video recorded at p = 2 bar, u_{in} = 65 m/s, λ = 1,69 and $P_{th,h}$ = 369 kW. The flame in this image has the conical structure that was typical for the visual appearance in all studied operating conditions. It partially extends into the burner mouth. This is due to the recirculation of the swirl flow. The flame can be described as lifted-off, because it does not touch the burner surface.

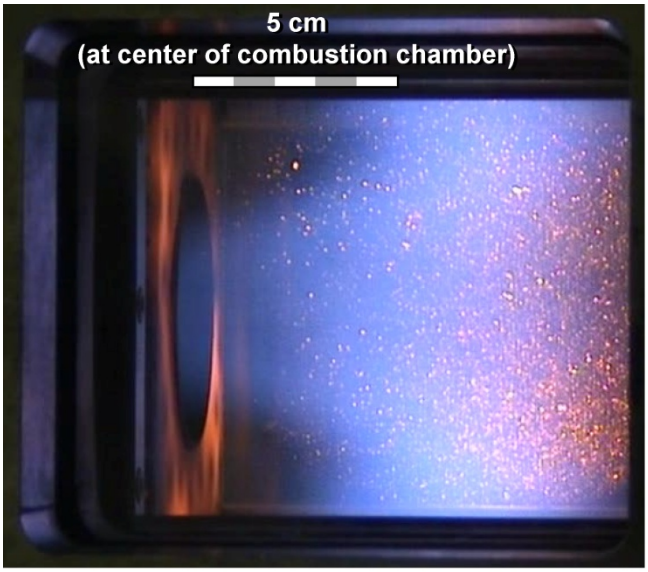

Fig. 3. Still image of an RGB video of a typical flame at the GT burner. The orange and red spots (white and light gray in printed version) are glowing impurities on the windows surface.

3. Results - Flow field

3.1. Comparison of isothermal with reacting case

Figure 4a shows a single shot result of the PIV measurement at operating condition "Iso" as a streamline plot. The burner nozzle is indicated by a bar on the z-scale. One of the most prominent features of this typical instantaneous flow field is the inflow zone with local planar flow speeds of up to ~20 m/s. In this publication, the term "inflow zone" shall be defined as a contiguous conical region of large positive axial velocity and outward directed radial velocity that is anchored at the burner. Another prominent feature in Fig. 4a with even higher local velocities expands along the symmetry axis of the combustor and has also a positive axial flow direction. This flow structure is assumed to be caused by a fast rotating central vortex core (CVC) that is believed to stretch down the whole way to the exhaust gas pipe. It is predicted by numerical simulations [38,60], and the interpretation as a CVC is consistent with the significantly decreased local seeding particle density that was observed in the raw images of the PIV measurement (not shown here). The particle density was still high enough for the PIV analysis. The occurrence of a CVC is not untypical for combustion chamber flow fields and was already observed by Heitor and Whitelaw [70]. The phenomenon is related to the Rankine vortex that appears in cyclonic combustors or separators [71,72]. In the ensemble averaged flow field of case Iso (see Fig. 4b) both features are reflected well. An asymmetry is seen in the central axial region of the ensemble averaged flow field. Its magnitude is higher than the estimated measurement error and it was present during the whole measurement campaign. It may be due to the small radius of the vortex core, its high revolution rate and a possible small geometrical asymmetry. As the vortex core is anchored at the exhaust gas pipe, the radial position of its upstream end is less stable. A small asymmetry of the combustor geometry or boundary conditions may therefore cause an offset of a few millimeters. Between the CVC and the inflow zone, an inner recirculation zone (IRZ) is established that has the shape of a hollow cone. In the instantaneous flow field, the IRZ reveals a different shape: it mainly consists of smaller vortices that appear in the inner shear layer (ISL). The latter can be defined as the conical layer with a mean axial velocity of zero. In the averaged flow field the superposition of these transient vortices forms the larger IRZ.

Figs. 4c and d show a typical instantaneous flow field and the ensemble average at reacting conditions (case A). The influence of the CVC on the observed part of the flow field is much smaller when combustion takes place, although it does not vanish completely. Statistically appearing spots with instantaneous flow speeds of 40 m/s and more that are located near the central axis (like at $x \approx 120$ mm, $z \approx 0$ in Fig. 4c) indicate that the upstream end of the CVC is still located in the PIV field of view. The shorter CVC in the reacting case leads to a different structure of the IRZ, which now has the shape of a large solid cone instead of a hollow cone. It reaches back into the burner nozzle and is associated with a high backflow rate of combustion products. The mean flow pattern in the inflow zone in the reacting case has a shape similar to the one in the isothermal case: The radial extents as well as the opening angle in the region of $x < 80$ mm are the same in both cases. There is also no difference between the two cases seen in the outer recirculation zone (ORZ) and the outer shear layer (OSL) that can be defined as the outer layer ($|z| > 43$ mm) in the vicinity of the burner ($x < 60$ mm) with the highest velocity gradients.

More details of the flow field of case A are displayed in Fig. 5 showing radial profiles of the mean and RMS values of the axial and radial velocity components. The profiles were extracted from the PIV images at those heights where also Raman measurements were performed. The prominent features of the profiles of the axial velocity are the inflow regions with high velocities and a pronounced IRZ with mean velocities on the order of -15 m/s at $x = 18.6$ mm. The RMS values increase slightly with distance from the burner and exhibit peaks in the inner and outer shear layers. Generally, the profiles of axial velocity have good axial symmetry. For the radial velocity (v), the axial symmetry is poor. While the positions and absolute values of the maxima of the mean radial velocity are quite symmetrically arranged at $x = 18.6$ and 38.6 mm, the values near the axis do not exhibit the expected behavior and this tendency becomes worse with increasing distance from the burner. As stated above, the central vortex core in conjunction with possible asymmetries of the boundary conditions may

contribute to this behavior. As a side note, in swirl flows deviations from axial symmetry are often observed because the flow field is very susceptible to slight disturbances.

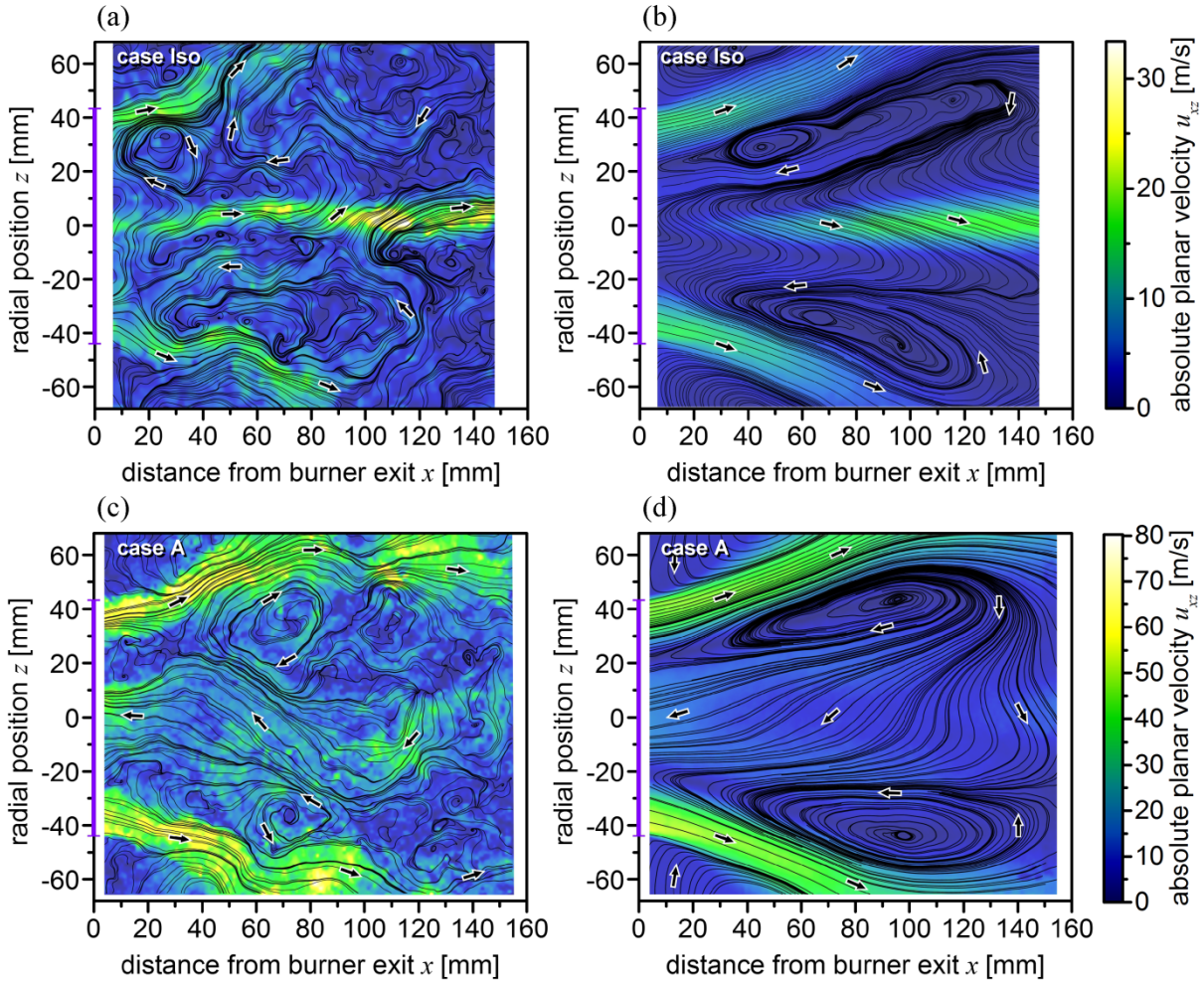

Fig. 4. Stream line plots of the instantaneous (left) and the ensemble averaged (right) flow fields of case Iso (a and b) and case A (c and d) with small arrows indicating the flow direction. The burner nozzle diameter is marked as a violet (printed: gray) bar on the *z*-scale. Note the different color bars. The number of instantaneous flow fields that were averaged for calculating the mean flow fields are 120 (case Iso) and 198 (case A) respectively.

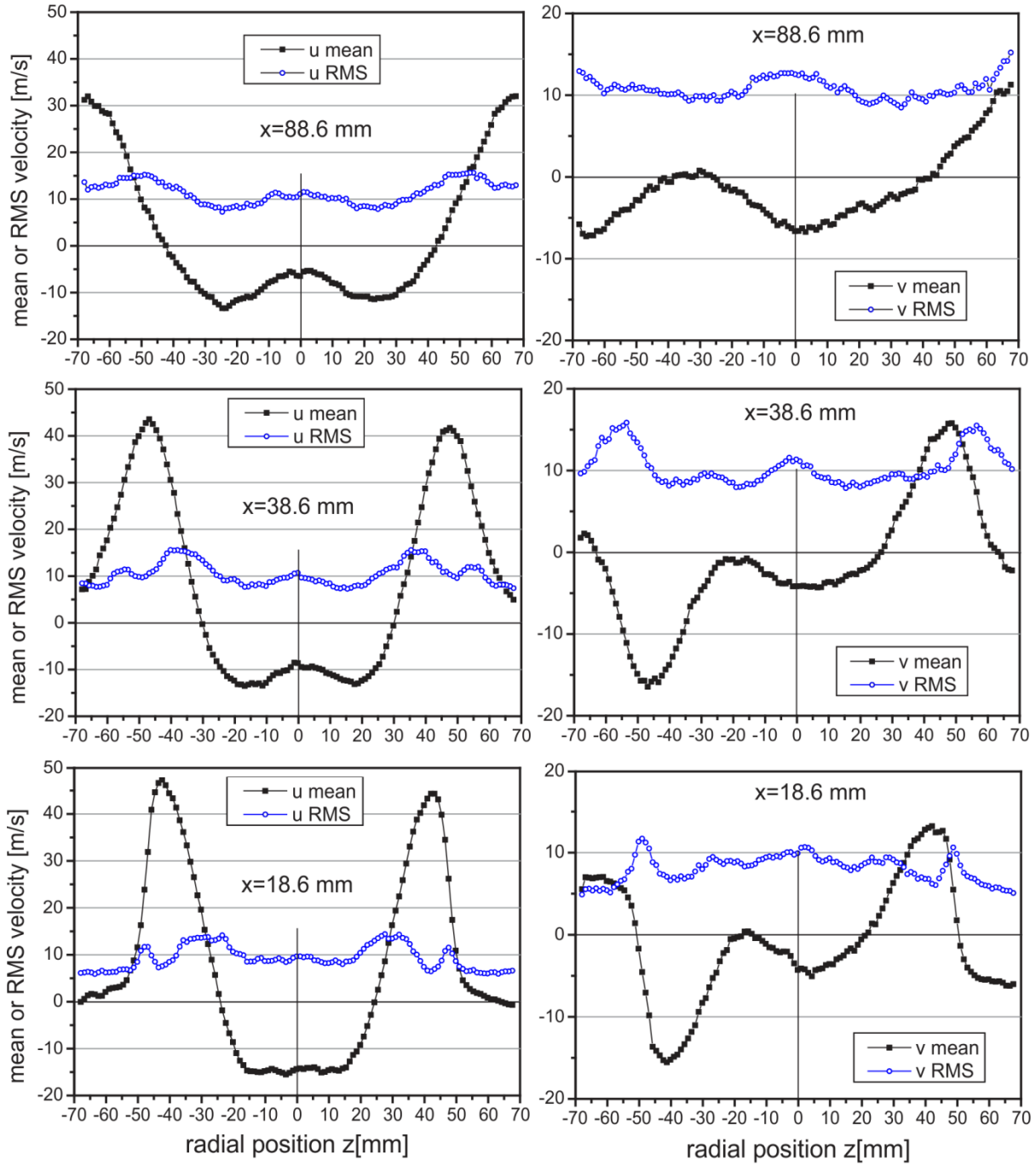

Fig. 5. Radial profiles of the mean and RMS values of the axial (u) and radial (v) velocity components of case A at different distances x from the burner.

3.2. Mapping of Strain Rate and Vorticity

The ensemble averaged total planar strain rate $\overline{\sigma}$ was calculated from the strain rate tensor $S_{ij} = (\partial_j u_i + \partial_i u_j)/2$ according to $\sigma = \left(\sum_{i,j} S_{ij}^2 \right)^{1/2}$. The sum successively assigns all relevant directions (here: only the two planar components x and z) to both of the indices i and j. The ensemble averaged out-of-plane component of the vorticity $-\overline{w_y}$ was calculated with the equation $w_y = \partial_x u_z - \partial_z u_x$.

Radial profiles of the ensemble average and the standard deviation of the total planar strain rate at x = 18.7 mm in case A are shown in Fig. 6. High levels of strain are seen in the vicinity of the ISL and the OSL. The maxima of the profiles coincide with the maxima of the profiles of u' at the same axial location (see Fig. 5). Adding the average value and the standard deviation, instantaneous strain rate values of more than 12 000 s^{-1} do not seem to be untypical in the OSL. Such high values occur in approximately 14 % of the samples, if a Poisson distribution is assumed. The regions of high strain in the OSL exhibit a smaller radial extension than in the ISL. This is explained by the presence of the edge of the burner nozzle at z = 43 mm which defines the beginning of the OSL. The position of the ISL is instead aerodynamically determined and subject to turbulent fluctuations. 2D mappings of the ensemble averaged total planar strain rate and the out-of-plane component of the ensemble averaged vorticity are displayed in Fig. 7 for the case A flame. It is seen that the regions of high strain become broader with increasing distance from the burner while at the same time the average peak strain rates decrease. The out-of-plane vorticity also exhibits the highest average values in the shear layers, as expected. In both distributions, the increased values near the flame axis are indications of the central vortex core (CVC). In the distributions of strain rates and vorticity of the case B flame (not shown here) the CVC is not so well pronounced. However, in general the distributions from case B are quite similar to those of case A.

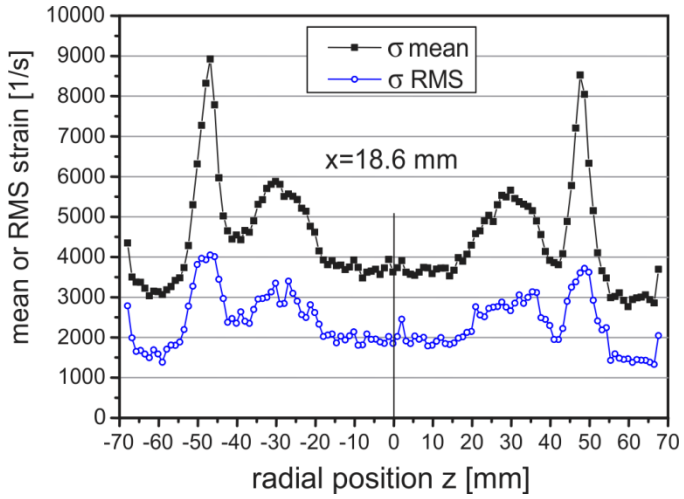

Fig. 6. Radial profiles of the ensembe average and the standard deviation of the total planar strain rate at x = 18.7 mm in case A.

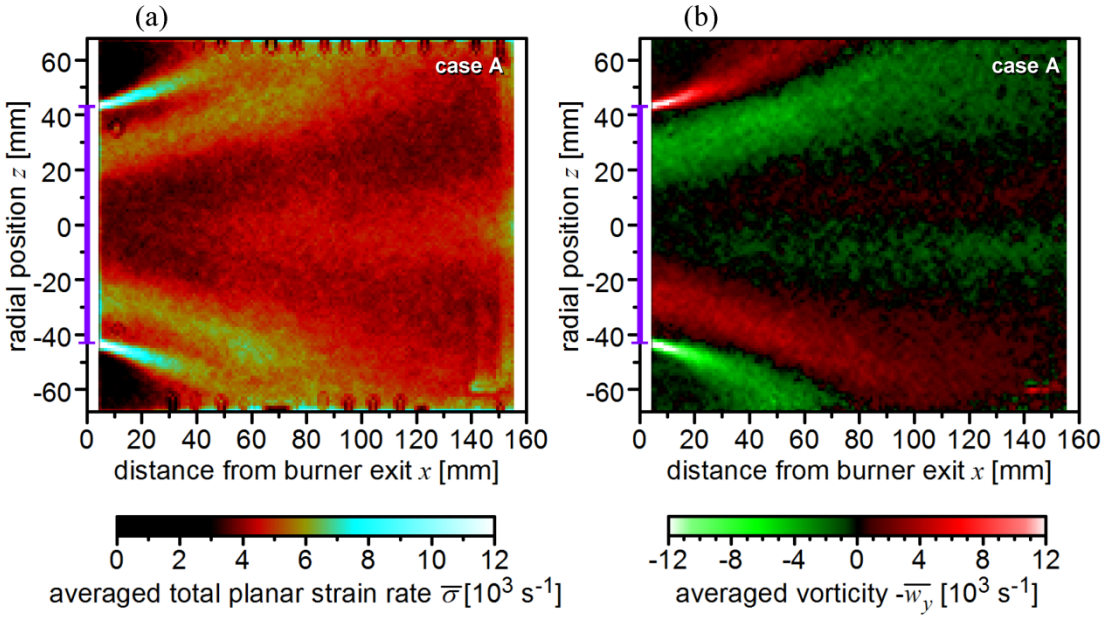

Fig. 7. Mappings of the ensemble averaged total planar strain rate (a) and the out-of-plane component of the ensemble averaged vorticity (b). The burner nozzle diameter is marked as a violet (printed: gray) bar on the z-scale. Periodic patterns at $|z| \geq 60$ mm are artifacts due to stray light. Every part figure shows the ensemble average of 198 instantaneous distributions.

3.3. Dependency of flow field and acoustics on stoichiometry, inflow velocity and pressure

At different operating conditions, the influence of the varied parameters on the flame or the flow field was studied. It was found that the equivalence ratio and the inflow velocity had no significant effect on the structure of the flow field like shapes and sizes of IRZ, inflow zone and ORZ. Of course, the absolute values of the velocities and thus the vector lengths changed. This leads to the conclusion that the mean flow field structure in the reacting cases is mostly predefined by the parameters of the combustor geometry, like the swirl number and the relative dimensions of the burner nozzle. At least for non-reacting flows this behavior can be expected, because at high Reynolds numbers the wall region with a significant viscous contribution to the shear stress is very thin. For example, above $Re \approx 2 \cdot 10^4$, the viscous wall region is thinner than 10 % of the half channel width [73]. A further increase of Re has no notable effect on the normalized mean velocity profile of the confined flow.

An influence of the pressure on periodic pressure oscillations of the flame is indicated by the results of the acoustic recordings, which show an increase of the measured pressure amplitude from 19 mbar at case A to 113 mbar at case B. The observed change of the acoustic frequency was small (209 Hz ± 19 Hz at 3 bar, 220 Hz ± 19 Hz at 6 bar) and possibly affected by systematic errors of the order of 10 Hz. In general, periodic pressure fluctuations inside combustion chambers are likely to change the shapes of the flow field and species distributions. In order to investigate the influence of pressure oscillations on the flow field of case B the results from the PIV measurements were assorted with respect to the measured pressure fluctuations in the combustion chamber. Phase angle 0° was defined as the zero crossing of $(p - p_{mean})$ when it changed from negative to positive values. Eight phase intervals were used with phase interval 1 ("ph 1") comprising the phase angles 0° - 45°, phase interval 2 ("ph 2") from 45° - 90° etc. After assigning the measured velocity values to phase intervals the mean values within each interval were calculated. These are termed phase-correlated mean values.

Figure 8 shows phase-correlated mean values of the axial and radial velocity components of case B for different phase intervals. The displayed radial profiles were extracted from the PIV measurements for $x = 19.3$ mm, close to the distance from the burner at which Raman measurements were performed. For clarity only 4 phase intervals are shown including the phases with the largest variations. The peak

values of the axial velocity do not vary much during an oscillation cycle, however, the width of the profiles changes and is at maximum at ph 2. The most prominent changes are seen for the IRZ where the mean values vary between approximately -10 m/s (ph 2) and -28 m/s (ph 6). The changes are symmetric with respect to the flame axis and indicate an axial motion of the IRZ. The profiles of the radial velocity show again a deviation from axial symmetry which, however, changes with phase interval. Besides this, phase-dependent variations are observed in the ORZ with minimal backflow at ph8. Here, the variations are not so well pronounced as in the IRZ, but they also indicate a symmetric motion with respect to the flame axis. The overall cyclic changes of the flow field are better seen in phase-correlated two-dimensional streamline plots illustrated in Fig. 9 for the phase intervals 2 and 6. The vortices seen in the inner shear layer are cuts through toroidal vortex structures. The larger one seen at ph 6 has a relatively constant position during an oscillation cycle. In addition, another vortex ring appears with each cycle at the burner mouth at around ph 4, moves downstream and finally merges with the larger one. This periodic vortex shedding is accompanied by changes in the flow velocities, particularly in the IRZ as shown before.

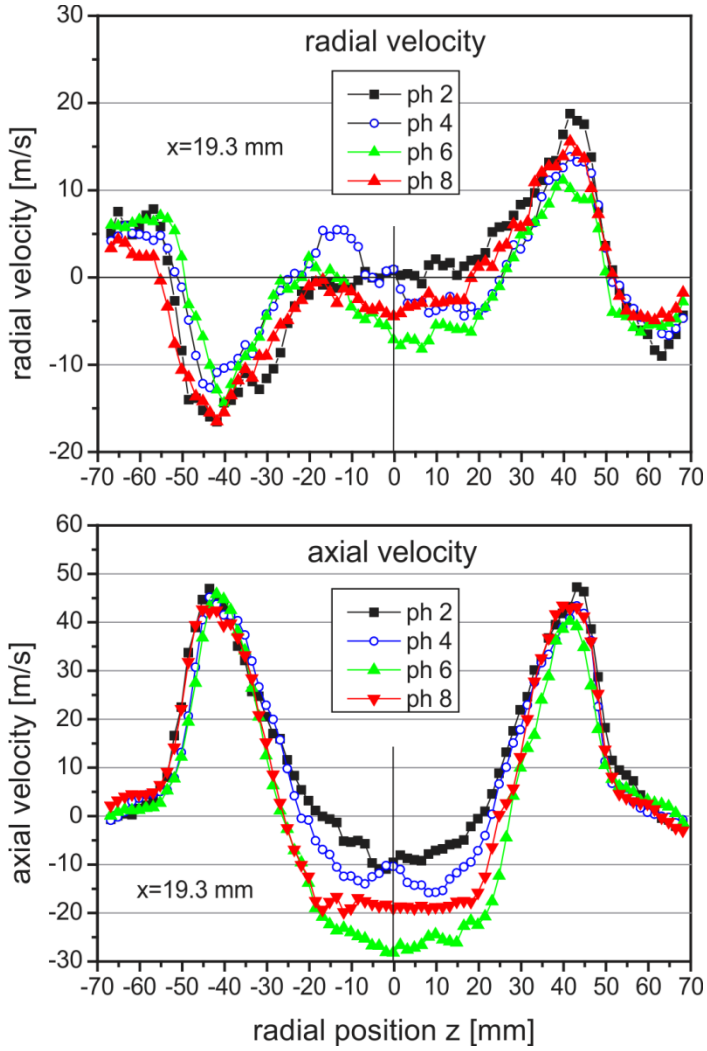

Fig. 8. Radial profiles of the mean phase-correlated radial and axial velocity components from case B flame for 4 different phase intervals.

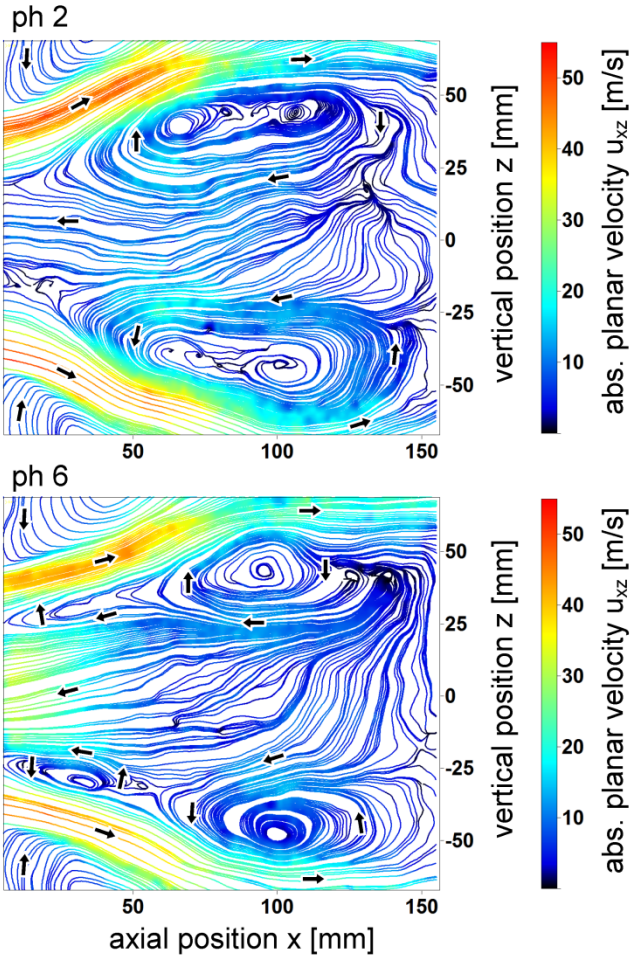

Fig. 9 Streamline plots of the phase-correlated mean flow field of case B at phase intervals 2 (top) and 6 (bottom). Small arrows indicate the local flow direction.

4. Results - Fuel/air premixing

4.1. Relevance and definition

The quality of the fuel/air premixing in the inflow zone is of significant relevance as spatial or temporal fluctuations of the equivalence ratio can cause increased NO_x emissions as well as thermoacoustic pulsations. Furthermore, developers of CFD tools need such validation data, because incorrect predictions of mixture fraction distribution and fluctuation can indicate a wrong modeling of the turbulence. In this study, the mixture fraction of each observation volume and each single shot was derived from the measured chemical composition. Similar to the definition by Bilger [74], it was calculated with the formula

$$f = \frac{2 \cdot \frac{Z_C}{m_C} + 0.5 \cdot \frac{Z_H}{m_H} - \frac{Z_O - Z_{O,a}}{m_O}}{2 \cdot \frac{Z_{C,f}}{m_C} + 0.5 \cdot \frac{Z_{H,f}}{m_H} - \frac{Z_{O,f} - Z_{O,a}}{m_O}}, \quad (1)$$

in which Z stands for the element mass fraction (averaged over all molecule species, weighted with their mole fractions), m stands for the atomic mass and the elements are specified with subscripts ”C”, ”H” and ”O”. An appended subscript ”a” or ”f” indicates that Z refers to the air or fuel stream instead of the gas in the observation volume.

4.2. Mean mixture fraction distribution

The time-averaged mixture fraction field is, of course, inhomogeneous in the vicinity of the fuel injection and becomes more homogeneous further downstream due to the mixing progress. However, depending on the burner geometry and the flow characteristics, inhomogeneities can still be present downstream of the burner exit.

For a visualization of the fuel-rich and fuel-lean regions in the time-averaged field, the ensemble averaged mixture fraction $\bar{f}$ is shown as a contour plot in Fig. 10. To avoid spatial averaging along the z axis, only the single shot results from the two central observation volumes (-0.29 mm < z < 0.29 mm) were included in the averaging. The contour plot therefore represents the horizontal symmetry plane of the combustor. It can be seen that the mixture fraction has significantly higher values in the radially outer region of the inflow zone, while the radially inner region of the inflow has leaner mixtures in the time average. The extremal values of the averaged distribution at case A are $\bar{f}_{\min}$ = 0.0260 and $\bar{f}_{\max}$ = 0.0334 corresponding to $\overline{\lambda}_{\max}$ = 2.24 and $\overline{\lambda}_{\min}$ = 1.73, respectively. The measured mixture fractions are significantly leaner than the global mixture fraction of $f \approx 0.0346$ that is calculated from the global air equivalence ratio of $\lambda \approx 1.67$ which is based on the preset fuel and air mass flows (see Table 2). One source for this discrepancy might be the inaccuracy of the mass flow meters (~4% for air and ~3% for fuel mass flows), another source the stated Raman measurement inaccuracy of $\Delta f \approx 0.003$. It is noted, that the contour plots in Fig. 10 do not cover the whole radial extent of the combustion chamber. Therefore, the values from the measured region do not necessarily reflect the overall mixture fraction. For case B the mean mixture fraction distribution is quite similar with slightly larger values of $\bar{f}$.

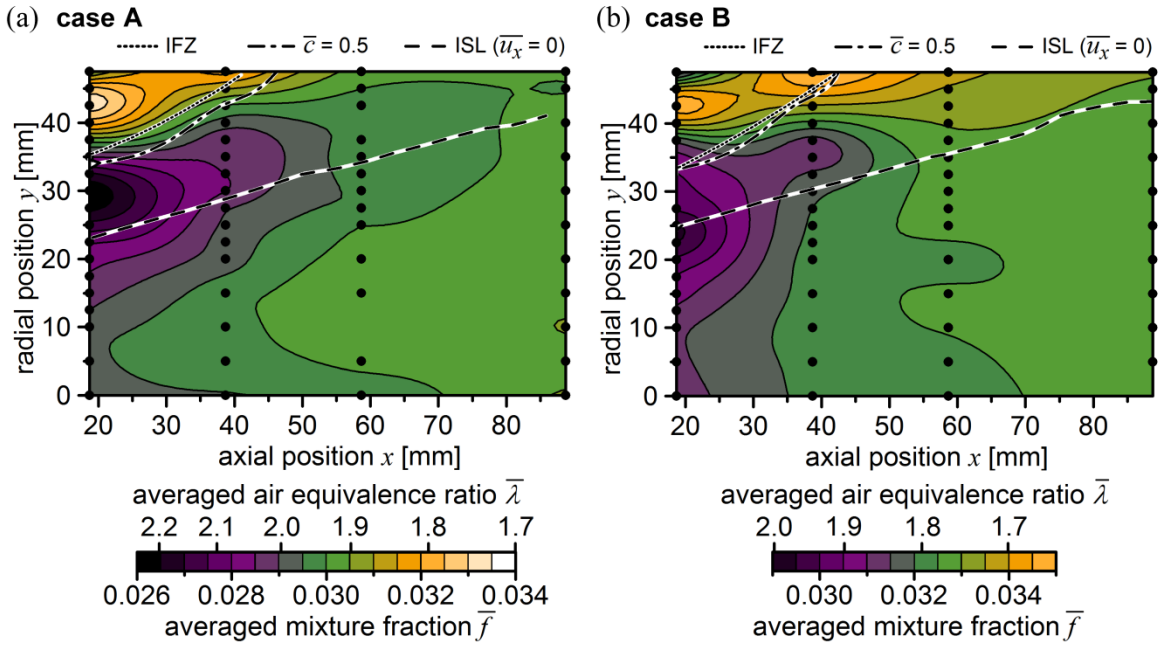

Fig. 10. Contour plot of the mean mixture fraction in the horizontal symmetry plane measured in the two central Raman observation volumes (–0.29 mm < z < 0.29 mm) in the flame of case A (a) and case B (b). Black spots represent the scanned x-y positions of the laser beam. For each position the results of 500 single shots were averaged. Broken lines indicate the inner shear layer, the layer with an average reaction progress of 0.5 and the inner flame zone (see section 5).

In order to illustrate the mixture fraction inhomogeneity and its variation during a thermo-acoustic cycle in more detail, Fig. 11 shows radial profiles of the mean mixture fraction and fuel mole fraction at x = 18.6 for cases A and B. For case B, phase-correlated mean values are displayed as described above. Again, only the single shot results from the two central observation volumes (-0.29 mm < z < 0,29 mm) were included in the averaging. Significant phase-dependent variations of the mixture fraction are seen in the radial region from about 30 mm to 48 mm which corresponds to the inflow zone of fresh gas. The mixture fraction variations correlate well with the variations of the fuel mole fraction. Peak values of $f \approx 0.05$ occurred around ph 4 and are significantly larger than the mean value. One reason for the cyclic variation of mixture fraction lies in the different impedances of the fuel and air supply lines. Pressure variations in the combustion chamber therefore influence the fuel and air mass flows differently resulting in equivalence ratio variations [2,16].

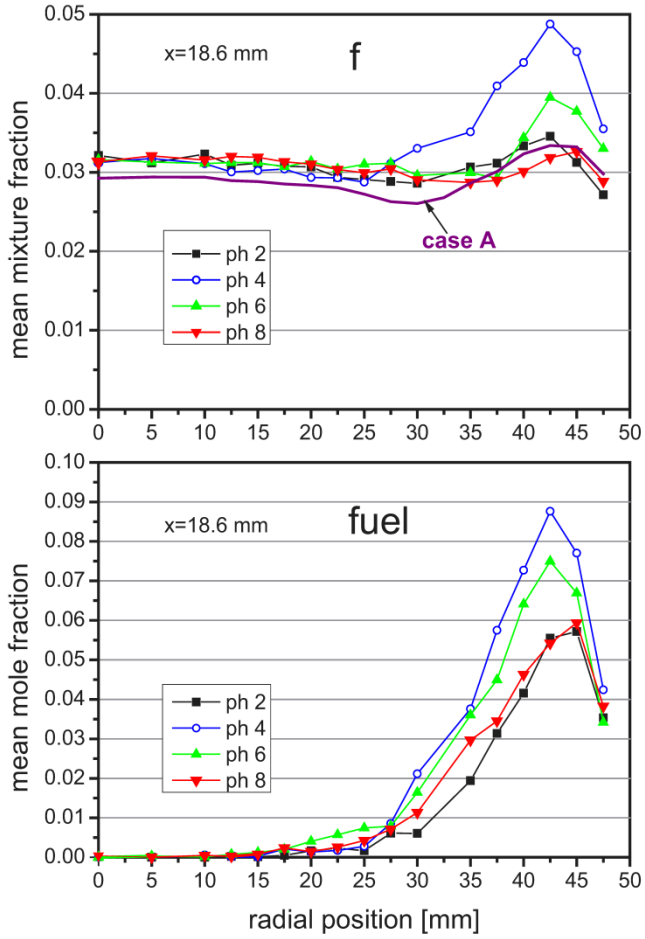

Fig. 11: Radial profiles of mean mixture fraction (top) and fuel mole fraction (bottom) in case A and B flames at 18.6 mm distance from the burner. For case B, phase-correlated mean values are displayed for 4 different phase intervals.

4.3. Small scale fluctuations of the local mixture fraction in the fuel/air mixture

Spatial and temporal variations of the mixture fraction can have an influence on the local burning characteristics like, e.g., flame anchoring, flame speed, local flame extinction, heat release rate or pollutant emissions. Also, the effect of mixture fraction gradients in premixed flames (i.e. stratified combustion) has currently gained increased attention with respect to turbulent flame models [75,76]. In the flames studied here, the variations in mixture fraction depend on the mixing progress on the way from the fuel injection within the swirler to the location under consideration. It is thus dependent on the turbulence level, burner geometry and residence time. Large scale variations of mixture fraction

are also influenced by thermoacoustic oscillations, with time and length scales given by the period and wavelength, respectively, of the oscillation.

An analysis of the instantaneous spatial mixture fraction fluctuations was performed by studying the instantaneous 8 mm long mixture fraction profiles along the laser beam. For each *x*-*y*-position and operating point 500 instantaneous 1D profiles were available. Because the primary goal was to study the premixing of fuel and air and not the mixing with products, only single shots from the inflow zone without reaction products (criterion: $X_{H2O} < 0.5$ vol.-%) were analyzed representing pure unburned fuel/air mixtures. The profiles were processed in the following way:

- Subtraction of the ensemble averaged profile from the *N* single shot profiles. This eliminates very slowly changing or temporally constant phenomena like lean/rich structures in the time-averaged field. The result is called "offset corrected mixture fraction" f^{oc}.
- Three-point-smoothing (sliding average) of the corrected single shot profiles to reduce the effect of readout and photon shot noise to about half of its original amplitude.
- Search for the maximum f^{oc}_{max} and the minimum f^{oc}_{min} of each smoothed single shot profile and calculation of the difference between both values: $\Delta f = f^{oc}_{max} - f^{oc}_{min}$. This single shot internal difference is not influenced by shot-to-shot variations with relatively long length scales like thermoacoustic pulsations. Instead, it only reflects the amplitude of the small scale spatial fluctuation in the instantaneous mixture fraction field of the given single shot.

Because of the three-point-smoothing, the Δf value contains only a small amount of statistical error from single shot internal noise. The results produced by the described method are only sensitive to mixture fraction fluctuations on length scales above ~0.6 mm (three-point-smoothing) and below 8 mm (observed beam section).

The evaluation of Δf at the location (x = 18.7 mm, y = 42.5 mm) for three different operating conditions (cases A, B and C) revealed no significant differences between these cases despite of the large differences in inflow velocity, pressure and *Re* number. The PDFs of Δf peaked at around $\Delta f_{max} \approx 0.014$ and had a half width of approximately $\Delta f_{FWHM} \approx 0.013$. It is noted that the number of samples was relatively small due to the quite low filter threshold of $X_{H2O} < 0.5$ vol.-%. It was 45, 123 and 63 for the cases A, B and C, respectively. Nevertheless, the result indicates that no significant improvement of the premixing is achieved by increasing the Reynolds number.

For each of the three operating conditions Fig. 12 shows a typical f^{oc} profile representing the median value of Δf and an f^{oc} profile with a relatively strong mixture fraction variation selected in a way that only about 5 % of the single shots in the ensemble have a higher Δf value. The measurement location was again x = 18.7 mm, y = 42.5 mm. The spatial variations displayed in the figure are significantly larger than the measurement uncertainty of approximately 0.003. In the inflow zone at x = 18.7 mm mixture fraction variations were always present. This was known before [52], however, in this study the scatter of the mixture fraction and its gradients could be determined quantitatively for the first time in an industrial GT burner (in a study at a scaled industrial burner the scatter of the mixture fraction was also quantified but that did not include the analysis of instantaneous mixture fraction gradients [20,77]. The observed mixture fraction variations lead to variations of the combustion temperature. If the typical value of $\Delta f \approx 0.014$ measured in the unburned gas is also present in the flame front, variations of the adiabatic flame temperature on the order of $\Delta T \approx 450$ K can occur. This would have an impact on the NO formation.

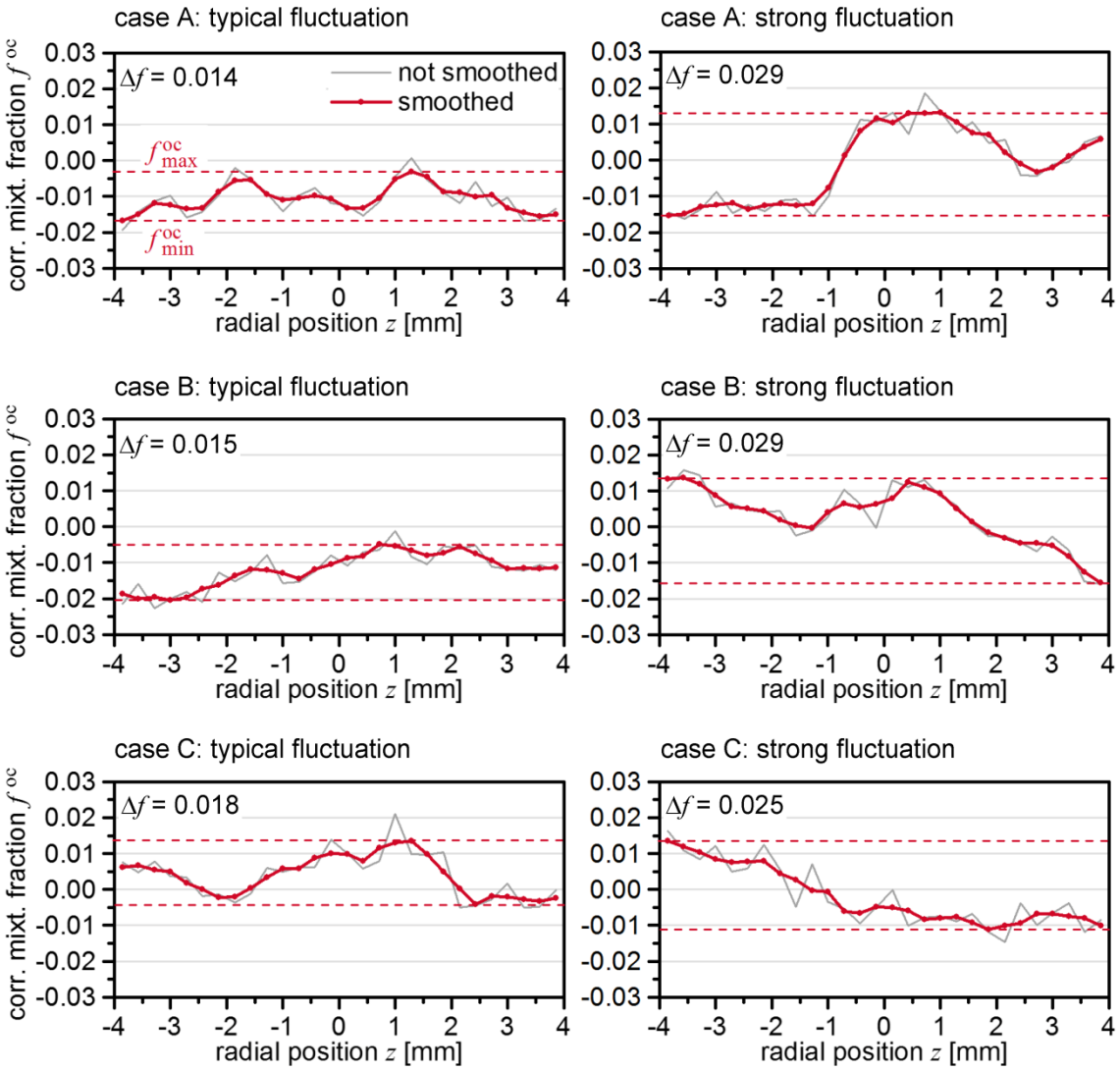

Fig. 12. Examples for typical (left) and relatively strong (right) instantaneous mixture fraction fluctuations at the three compared cases (x = 18.7 mm, y = 42.5 mm). The typical profile always represents the profile with the median Δf value in the ensemble. Only 5 % of the single shots in each ensemble have a higher Δf value than the shown example for a ”strong” fluctuation.

5. Results - Combustion process

5.1. Shapes of the instantaneous flame front and the averaged flame zone

The results from the OH PLIF measurements provide qualitative information about the instantaneous distribution of OH radicals within the vertical symmetry plane of the combustion chamber. Detectable amounts of OH radicals are present in the reaction products at temperatures above ~1400 K. The results are only qualitative, because absorption effects lead to systematic errors in the PLIF images like the vertical asymmetry of the signal distributions in Fig. 13. Part (a) of the figure shows a typical PLIF single shot of case A. The blue and purple (b/w-printed: dark gray) zones reflect hot reaction products. The black zones indicate the inflow of the unconsumed fuel/air mixture. Orange and yellow (printed: light gray) areas are caused by super-equilibrium concentrations of OH that exist for only a few milliseconds (or less at higher pressure) immediately after the OH formation in the flame front. The steep gradient in the PLIF signal between the inflowing fresh gas and the super-equilibrium OH concentrations is therefore a good marker for the location of the flame front. It can be visualized by applying Sobel filters to the PLIF results. The filtered PLIF single shot is shown in Fig. 13b. The

corrugation of the flame front by the turbulence is clearly visible in these single shots. If all 200 single shots recorded at one operating point are Sobel-filtered and then ensemble averaged, the result is a qualitative mapping of the probability density function (PDF) of the flame front location (see Fig. 13c). It is noted that in the averaged distribution all gradients of the OH PLIF distribution were taken into account. The small ones do not necessarily represent flame fronts but may stem from the decay of super-equilibrium OH towards chemical equilibrium. The image shows that the reactions in the flame of case A start in two separate zones, the inner flame zone (IFZ) and the outer flame zone (OFZ), that are divided by the relatively cold fresh gas inflow for $x < 40$ mm. Further downstream both zones merge. In Fig. 13c, the maxima of the two zones are marked by dotted lines, which correspond to the maxima of the radial PDF of the flame front location. The IFZ expands upstream to locations with $x < 0$ which means that a significant amount of reactions takes place inside the burner nozzle. The OFZ is detached from the burner nozzle exit by a distance of approximately 5 – 10 mm where the inflowing fuel/air mixture obviously does not react although it must already be in contact with hot reaction products from the ORZ. At an average inflow velocity of ~40 m/s, this distance corresponds to a time interval of approximately 100 – 300 µs. This is of the same order as the expected ignition delay time at temperatures of 1400 – 1700 K [78,79]. The PDF of the flame front location changes, when the pressure in the combustion chamber is increased, as can be seen in Figs. 13d–f that show the same results for case B. At this operating point, fewer reactions take place in the OFZ, while the inner zone with a high flame front occurrence frequency is radially extended towards the combustor axis. Also the corrugation of the instantaneous flame front is significantly increased at higher pressures. In the displayed single shot image of case B and its gradient mapping the flame front appears to be disrupted at some points. This could be due to events of local flame ignition and extinction, though the cut of the laser sheet through a three-dimensionally connected flame front can produce a similar effect. By roughly estimating the laminar unstretched flame speed (0.33 – 0.50 m/s, [80]) as well as the laminar unstretched flame front thickness (240 – 330 µm, [81] with diffusion coefficients from [82]) and by calculating the standard deviation of the velocity from the PIV measurements in the ISL, Damköhler numbers of $Da \approx 1.4 – 2.5$ and Karlovitz numbers of $Ka \approx 77 – 230$ can be deduced for the flames of the cases A – D. According to the regime diagrams by Borghi [83] and Peters [81], thickened flame fronts and local extinctions are to be expected in these flames.

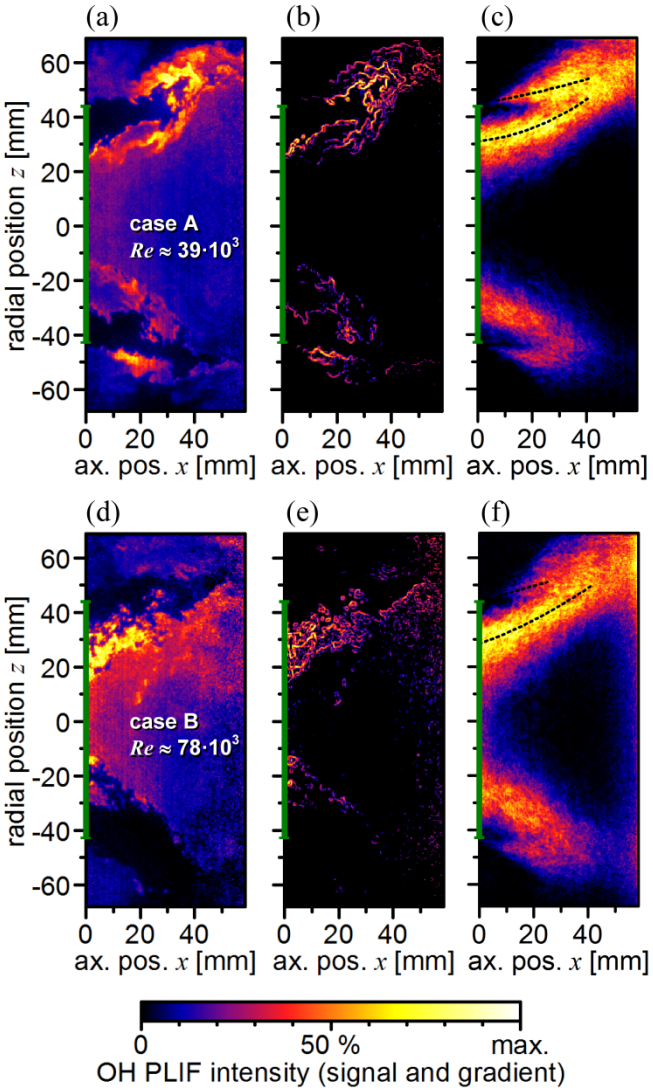

Fig. 13. Mappings of the instantaneous OH PLIF intensity (a and d), its gradient (b and e) and the ensemble average of its gradient (c and f, averaged over 200 single exposures) for cases A (upper row) and B (lower row). The burner nozzle diameter is marked as a green (printed: grey) bar on the *z*-scale. Dotted lines mark the inner and the outer flame zone of case A (c).

5.2. Average location of the heat release

In many investigations, OH* chemiluminescence imaging is used to characterize the flame zones because it is a quite simple diagnostic technique compared to PLIF. Therefore, results from OH* chemiluminescence imaging are presented here and opposed to the OH PLIF images. OH* radicals are produced in the flame front by exothermal chemical reactions. In the described experiment, the mean lifetime of the excited state is in the order of 0.1 ns - 1 ns [84]. Because of this short time span, a high local OH* chemiluminescence signal is a good indicator for a high amount of heat being released by the reactions. Due to the pressure dependent quenching rate, signal trapping and the signal integration along the line of sight, chemiluminescence measurements provide only qualitative results. For a proper localization of the averaged zone of heat release, the chemiluminescence single exposures were ensemble averaged and then deconvoluted by an inverse Abel transformation [85]. The result is a qualitative two-dimensional mapping of the averaged local OH* concentration within the *x*-*z*-plane that also represents the averaged flame zone. Such cross-sectional views through the flame zones of the cases A and B are shown in Fig. 14. It is seen that the largest part of the heat is released between 3 and 7 cm downstream of the burner exit. The upstream end of the flame zone is split-up into two parts.

A smaller one located in the OFZ and a larger one in the IFZ. Between both, the inflow of unburned fresh gas is visible as a gap with low chemiluminescence intensity. In contrast to the PLIF results shown in Fig. 13c, the chemiluminescence signal in the IFZ appears to be significantly weaker in the region upstream of $x \approx 20$ mm. This signal decrease towards the burner nozzle is likely an artifact of the Abel transformation which only works properly if the line-of-sight is exactly perpendicular to the image plane. Using a normal imaging lens there is always a solid angle of detection that can lead to distortions of the reconstruction by an Abel transformation. Nevertheless, the good agreement between the radial flame zone locations that are seen in the PLIF measurements and the chemiluminescence measurements indicates that the Abel-inverted chemiluminescence images are useful for measuring properties like the opening angle or the diameter of the toroidal flame zone. An increase of the pressure from 3 to 6 bar leads only to a slight decrease of the lift-off height. This is made visible by marking the axial locations of the global signal intensity maximum and the upstream end of the flame zone in the inflow in Fig. 14. Possible explanations for this effect can be the decreased ignition delay time and the increased turbulent flame speed at higher pressures.

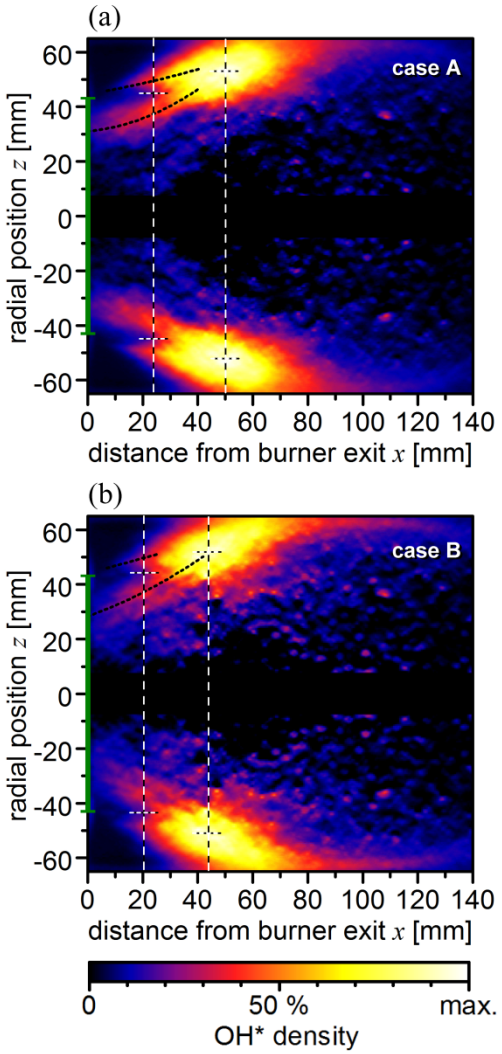

Fig. 14. Mappings of the deconvoluted intensity of the mean OH* chemiluminescence (ensemble average over 200 single exposures) at cases A (a) and B (b). Dashed lines and crosses indicate the end of the non-reacting inflow zone and the spots with the maximum heat release. Dotted lines mark the inner and the outer flame zone (a).

5.3. Statistics of the local thermochemical state

A series of 500 single shot measurements with 28 simultaneously observed volumes at a particular *x*-*y*-location results in a statistical basis of 28 × 500 = 14000 data points describing the thermochemical states at this location (with -4 mm < *z* < 4 mm). As an example, Fig. 15a shows a contour plot of a two-dimensional histogram with the local instantaneous temperature *T* and the mixture fraction *f* as the histogram variables. It shows the statistical distribution of a data set with 14000 points recorded in the IFZ (*x* = 18.7 mm, *y* = 32.5 mm) of the case A flame. Contour lines indicate the probability density φ within the *T*-*f*-space relative to the global maximum of the distribution (with a spacing of 10 % between the lines and a dotted line marking the 50 % level). The area enclosed by the φ = 10 % line is filled with colors representing the reaction progress *c* averaged over all data points in the particular histogram bin. The size of the histogram bins is about equal to the statistical measurement error at low temperatures. *c* was calculated from the measured species concentrations *X* and the mixture fraction *f*:

$$c = \frac{1}{2}\left(\frac{X_{\mathrm{H2O}}}{X_{\mathrm{H2O}}^{\mathrm{prod}}(f)} + 1 - \frac{X_{\mathrm{NG}}}{X_{\mathrm{NG}}^{\mathrm{react}}(f)} \right). \qquad (2)$$

$X_{\mathrm{H2O}}^{\mathrm{prod}}$ is the concentration of H_2O in the products at adiabatic equilibrium and $X_{\mathrm{NG}}^{\mathrm{react}}$ is the natural gas concentration in the unburned reactants. Both quantities are functions of *f*. Figure 15a shows a bimodal distribution with one maximum of φ close to the reaction products at the adiabatic flame temperature and the other one close to the line representing the unburned fuel/air mixture. Obviously, both types of gas can be present at the investigated *x*-*y*-position in the shear layer. Some single shot profiles (not shown here) indicate that products and reactants can be present at the same time in the 8 mm long beam section. Between the two maxima, a significant frequency of intermediate thermochemical states was found. The φ value for data points with $c \approx 0.5$ reaches 40 % in the ISL of the case A flame. Such intermediate states inside the observation volume (with the size of ~0.08 mm³) are characterized by medium temperatures and mixtures of air, fuel and combustion products. A discussion about their origin (published in [65]) comes to the conclusion that the two most relevant situations in which intermediate states are observed are when the laser beam is either crossing a flame front or a mixing layer in which reactants and products are blended before reaction occurs.

Figure 15b shows the same histogram for a measurement location in the OFZ (*x* = 18.7 mm, *y* = 47.5 mm). It reveals a much higher probability for the occurrence of intermediate states with a φ value of up to 80 % for $c \approx 0.5$. The two maxima of the bimodal distribution are barely separable in the OFZ. One reason for this difference is that the location of the boundary layer between the inflowing fresh gas and the recirculated products is less stable in the IFZ because its position is not directly predefined by the burner geometry as it is in the OFZ. A higher stability means a smaller variation range of the layer position and therefore a higher probability of being captured by the laser focus. Another reason for the high frequency of intermediate states in the OFZ is the fact that the outer part of the inflowing stream of fresh gas is not in contact with the hot recirculated products until it exits the burner nozzle. At the exit, the fresh gas starts to mix with the products. Before the ignition delay time is over, the gas reaches an intermediate state that can be still present at the measurement position in the OFZ. The proximity of the *x*-*y*-location represented by Fig. 15b to the not reacting region upstream of the OFZ at $0 < x < 10$ mm / $y \approx 45$ mm in Fig. 13c supports this assumption.

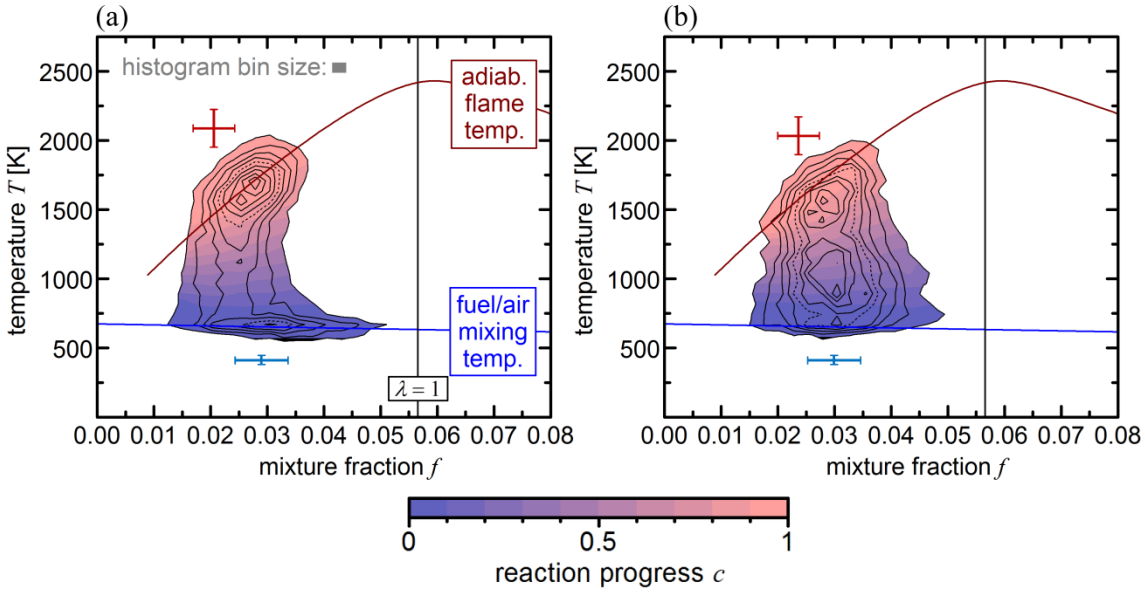

Fig. 15. Contour plots of the 2D histograms showing the probability density φ of the thermochemical state in the *T*-*f*-space for a position in the inner flame zone (a) and one in the outer flame zone (b) of case A. The spacing between the contour lines is $\Delta\varphi$ = 10 % of the maximum probability density value (100 %) in each histogram. The line at φ = 50 % is dotted. The area of φ > 10 % is filled with a color indicating the measured reaction progress *c* (ensemble average of the samples in the particular histogram bin). Each part figure represents the data of 14 000 point measurements (500 single shots with 28 observation volumes). The error bars represent the total errors of one single point measurement in the hot reaction products (upper cross) and in the unburned fuel/air mixture (lower cross) respectively.

5.4. Mapping of the mean and RMS temperature distribution

Two contour plots in Fig. 16 show the two-dimensional distributions of the ensemble averaged temperature values measured by Raman spectroscopy and the corresponding standard deviations. The figure represents a cut along the central *x*-*y* plane through the flame. To avoid a spatial averaging along the *z* axis, only samples from the two central observation volumes (–0.29 mm < *z* < 0.29 mm) were processed here. It should be kept in mind that the combustor wall is at *y* = 82.5 mm and that the Raman measurements covered only the radial range up to *y* = 47.5 mm. In the OH PLIF and OH* chemiluminescence images shown above it is seen that the flame zone extends beyond the area displayed in Fig. 16. However, the inflow region and the inner flame zone are captured. The locations of the ISL, the IFZ and the layer with an ensemble averaged reaction progress of $\overline{c}$ = 0.5 are included in the figure to facilitate the comparison of the results from three different diagnostic methods. It is seen, that the layer with the intermediate reaction progress nearly coincides with the IFZ, while the ISL is located closer to the combustor axis. Also, the opening angles of the IFZ, the layer with $\overline{c}$ = 0.5 and the temperature contour lines above 1000 K are practically identical, whereas the ISL has a significantly smaller opening angle

The smallest relative RMS values are present in the IRZ close to the combustor axis and far away from the burner. There, the measured temperature standard deviation was only about 6 % of the mean local value, which is even lower than the measurement precision specified in this paper for “typical” measurements (see Table 1). The temperature fluctuations in the exhaust gas are therefore below the detection limit. A comparison between case A and case B reveals an increase of the product temperature by approximately 100 K when the pressure is increased. This may be caused by less heat loss at higher pressures and partly by measurement uncertainty. The small temperature peak at $y \approx 24$ mm, x = 18.7 is likely an artifact from the raw data analysis described in Section 2.2. At that position the temperature reference value was switched from cold unburned gas to completely reacted gas at

adiabatic flame temperature. The RMS temperature fluctuations in the IFZ are significantly higher in case B. This is mainly due to the phase-dependent temperature variations induced by the thermo-acoustic oscillation. These are most prominent in the region of the IFZ where the phase-correlated mean values vary by up to approximately 400 K. However, the overall time-averaged shapes of the temperature distributions of case A and B are quite similar, i.e. the average shape is only weakly influenced by the thermo-acoustic oscillation. The same behavior was observed for the distributions of the species concentrations.

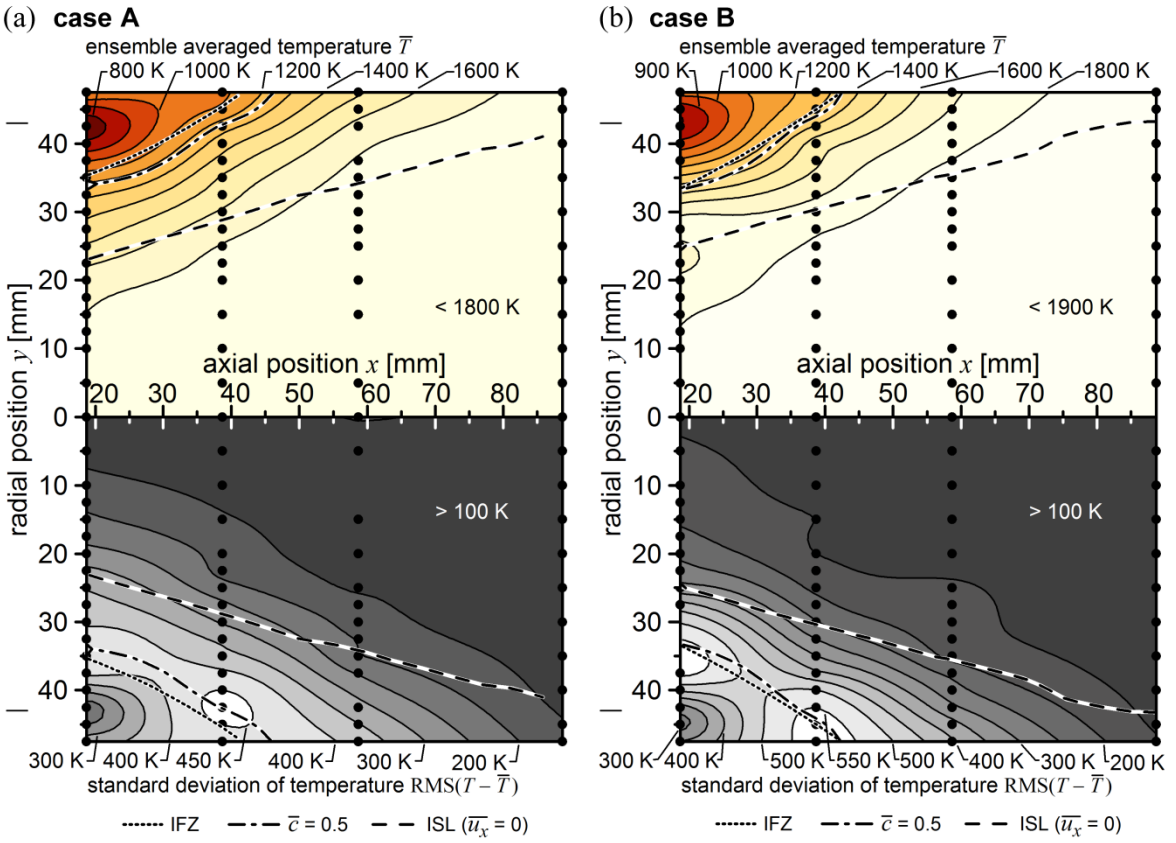

Fig. 16. Contour plots of the mean temperature and the standard deviation in the horizontal symmetry plane based on the total number density measured in the two central Raman observation volumes (–0.29 mm < z < 0.29 mm) in the flame of case A (a) and case B (b). Black spots represent the scanned x-y positions of the laser beam. For each position the results of 500 single shots were averaged to get the mean mixture fraction. Two marks on the left side indicate the burner nozzle diameter. The inner shear layer (ISL), the layer with $\overline{c}$ = 0.5 and the inner flame zone (IFZ) are represented by broken lines.

6. Summary and conclusion

An industrial gas turbine combustor for swirled premixed natural gas/air flames has been equipped with an optical combustion chamber and installed into a high-pressure test rig. Different flames with thermal powers up to 1.08 MW and pressures up to 6 bar as well as non-reacting flows have been studied using a variety of measurement techniques. The results include flow velocities obtained by PIV, flame structures from chemiluminescence imaging and PLIF of OH, joint PDFs of temperature, mixture fraction and major species concentrations from Raman measurements as well as data from dynamic pressure transducers and exhaust gas analysis. The main goals of the investigations were a better understanding of the combustion behavior of GT flames and the establishment of a comprehensive experimental database for the validation of numerical simulations.

The flow field structures of the non-reacting flows differed significantly from those of the reacting flows, for example regarding the length of the observed central vortex core. Parameter variations in the reacting flow had nearly no influence on the flow field structure. The 1D single-shot Raman measurements enabled the quantification of the degree of pre-mixing and the determination of gradients in the mixture fraction distribution. Due to the limited residence time available for mixing of fuel and preheated air, perfectly premixed combustion could not be achieved in this burner (as in all real GT burners). A detailed characterization of the mixing state and mixture fraction distribution was performed. This is important for a correct evaluation of the combustor performance and is needed for a comparison with numerical simulations. Fuel-rich and fuel-lean regions were found in the inflow zone of the averaged mixture fraction field. The analysis revealed that neither the pressure nor the inflow velocity had a significant influence on the statistics of the instantaneous mixture fraction fluctuations of the inflowing fuel/air mixture on length scales between ~ 0.6 and 8 mm. This range is dominated by randomly appearing pockets of relatively lean or rich gas. Such random pockets were found to cause mixture fraction variations of $\Delta f \approx 0.014$ in typical situations and $\Delta f \approx 0.027$ in situations with very strong fluctuations (stronger than 95 % of the analyzed profiles). These values did not significantly change when *Re* was changed. Apparently, the quality of the turbulent premixing is quite insensitive to variations of the operating point, at least for the variations studied here.

The case B flame exhibited thermo-acoustic oscillations. Phase-correlated measurements in this flame revealed a periodic vortex shedding at the burner mouth in connection with a significant variation of the backflow of burned gas within the inner recirculation zone. In the inflow zone close to the burner significant periodic variations of the mixture fraction were measured which are attributed to the different response of the fuel and air supply lines to the pressure oscillations in the combustion chamber.

The flame shape and the reaction zones could be visualized by planar laser-induced fluorescence of OH and the determination of the gradients of the OH distributions. The measurements revealed a strong influence of the operating parameters on the corrugation of the flame front. At moderate *Re* numbers, reactions zones were contiguous over several centimeters while at high *Re* numbers the flame appeared fragmented and exhibited small spatial structures. From the current experimental results it cannot be decided whether auto-ignition plays a significant role in flame stabilization at high *Re* numbers. At low *Re* numbers, it seems that the flame is mainly burning by the propagation of a turbulent flame front. The main region of flame stabilization and combustion is located in an inner flame zone between the inflow and the inner recirculation zone. The flame root was located within the burner mouth, upstream of the optically accessible region. At some operating conditions, combustion was also observed in an outer flame zone between inflow and outer recirculation zone, however, the flame was not anchored at the burner exit. The OH* chemiluminescence distributions were in agreement with the OH PLIF gradient images, but they did not so clearly show that the inner part of the flame zone reached upstream into the burner mouth. It is conjectured that the Abel-inverted chemiluminescence distributions do not reliably reflect the real OH* intensities in the outer parts of the field-of-view like the burner vicinity, because the Abel transformation is only defined for parallel and not for perspective projections. The distributions of mean and RMS temperatures revealed that the inner recirculation zone presents a large region of high temperatures with fluctuations smaller than the measurement precision. The largest RMS fluctuations were measured in the layer of the inner flame zone. The outer flame zone was hardly accessible by the Raman measurements due to the optical setup of the Raman experiment.

The reaction progress was also captured by the Raman measurements. The 2D histograms of temperature and mixture fraction revealed a large variation of the thermochemical states of the flames. Besides non-reacted and completely reacted samples, all possible intermediate states were observed, predominantly in the shear layers. Most likely the majority of the samples with intermediate temperature and reaction progress present mixtures of hot exhaust gas and fresh fuel/air mixtures. These mixtures have not reacted yet because either the residence time was not long enough for auto-ignition or they have not yet come in contact with a flame front. Obviously there is considerable mixing of fresh and exhaust gas before the burnout is completed. This behavior did not significantly

change with the operating conditions. Similar distributions of the reaction progress have previously been observed for swirl flames at atmospheric and elevated pressures [16,24,86].

All results have been integrated in an experimental database that gives a comprehensive and detailed description of the studied flames. Its main purpose is the validation of numerical simulations.

7. Acknowledgements

The experimental work was partially funded by the state of Baden-Württemberg through the KW21 research network. The authors would like to thank H. Ax, A. Bonaldo, E. Buchanan, I. Boxx, K.-H. Ferst, M. Kapernaum, I. S. Kim, P. Kutne, W. Krebs, R. Lückerath, R. Noden, U. Prestel, R. Tresch, S. Sadasivuni, V. Sanderson, K. Syed, L. Wehr, J. Zerbs and V. Zöller for their help and their contributions to the TurChemi/TCWW project.

References

[1] Y. Huang, V. Yang, Prog. Energy Comb. Sci. 35 (2009) 293-364.

[2] T.C. Lieuwen, V. Yang (Eds.), Combustion instabilities in gas turbine engines, in: F.K. Lu (Ed.), Progress in Astronautics and Aeronautics 210, American Institute of Aeronautics, 2005.

[3] K. Kohse-Hönighaus, J. Jeffries (Eds.), Applied Combustion Diagnostics, Taylor and Francis, New York, 2002.

[4] K. Kohse-Höinghaus, R.S. Barlow, M. Aldén, J. Wolfrum, Proc. Combust. Inst. 30 (2005) 89-123.

[5] A.M. Steinberg, C.M. Arndt, U. Stopper, W. Meier, 50th AIAA Aerospace Sciences Meeting 2012, AIAA 2012-0689.

[6] B. Böhm, C. Heeger, R.L. Gordon, A. Dreizler, Flow Turbul. Combust. 86 (2011) 313-341.

[7] M. Tanahashi, S. Taka, M. Shimura, T. Miyauchi, Exp. Fluids 45 (2008) 323-332.

[8] I. Boxx, M. Stöhr, C. Carter, W. Meier, Combust. Flame 157 (2010) 1510-1525.

[9] C. Heeger, R.L. Gordon, M.J. Tummers, T. Sattelmayer, A. Dreizler, Exp. Fluids 49 (2010) 853-863.

[10] D. Galley, S. Ducruix, F. Lacas, D. Veynante, Combust. Flame 158 (2011) 155-171.

[11] A.M. Steinberg, I. Boxx, C.M. Arndt, J.H. Frank, W. Meier, Proc. Combust. Inst. 33 (2011) 1663-1672.

[12] T.R. Meyer, M.S. Brown, S. Fonov, L.P. Goss, J.R. Gord, D.T. Shouse, V.M. Belovich, W. M. Roquemore, C.S. Cooper, E.S. Kim, J.M. Haynes, 38th AIAA/ASME/SAE/ASEE Joint Propulsion Conference and Exhibition 2002.

[13] F. Biagioli, F. Güthe, B. Schuermans, Exp. Thermal Fluid Sci. 32 (2008) 1344-1353.

[14] M. Stöhr, I. Boxx, C. Carter, W. Meier, Proc. Combust. Inst. 33 (2011) 2953-2960.

[15] B. Schürmans, V. Bellucci, F. Güthe, F. Meili, P. Flohr, C.O. Paschereit, Proc. ASME Turbo Expo 2004, GT2004-53831.

[16] W. Meier, P. Weigand, X.R. Duan, R. Giezendanner-Thoben, Combust. Flame 150 (2007) 2-26.

[17] P. Palis, D. Durox, T. Schuller, S. Candel, Combust. Flame 157 (2010) 1698-1717.

[18] S.K. Dhanuka, J.E. Temme, J.F. Driscoll, J. Propulsion Power 27 (2001) 631-641.

[19] P. Griebel, P. Siewert, P. Jansohn, Proc. Combust. Inst. 31 (2007) 3083-3090.

[20] R. Lückerath, O. Lammel, M. Stöhr, I. Boxx, U. Stopper, W. Meier, B. Janus, B. Wegner, Proc. ASME Turbo Expo 2011, GT2011-45790.

[21]P.A. Strakey, S. D. Woodruff, T.C. Williams, R.W. Schefer, AIAA J. 46 (2008) 1604-1613.

[22] J. Fleck, P. Griebel, A.M. Steinberg, M. Stöhr, M. Aigner, Proc. ASME Turbo Expo 2011, GT2011-45195.

[23] B. Janus, A. Dreizler, J. Janicka, Proc. Combust. Inst. 31 (2007) 3091-3098.

[24] H. Ax, U. Stopper, W. Meier, M. Aigner, F. Güthe, J. Eng. Gas Turbines Power 132 (2010) 051503.

[25] O. Lammel, H. Schütz, G. Schmitz, R. Lückerath, M. Stöhr, B. Noll, M. Aigner, M. Hase, W. Krebs, Proc. ASME Turbo Expo 2010, GT2010-23385.

[26] M.P. Thariyan, A.H. Bhuiyan, S.E. Meyer, S.V. Naik, J.P. Gore, R.P. Lucht, Meas. Sci. Technol. 22 (2011) 015301.

[27] F. di Mare, W.P. Jones, K. Menzies, Combust. Flame 137 (2004) 278-294.

[28] L. Selle, G. Lartigue, T. Poinsot, R. Koch, K.-U. Schildmacher, W. Krebs, B. Prade, P. Kaufmann, D. Veynante, Comp. & Fluids 137 (2004) 489-505.

[29] A.X. Sengissen, A.V. Giauque, G.S. Staffelbach, M. Porta, W. Krebs, P. Kaufmann, T. Poinsot, Proc. Combust. Inst. 31 (2007) 1729-1736.

[30] P. Schmitt, T. Poinsot, B. Schuermans, K.P. Geigle, J. Fluid Mech. 570 (2007) 17-46.

[31] C. Duwig, L. Fuchs, Phys. Fluids 19 (2007) 075103.

[32] J. Galpin, A. Naudin, L. Vervisch, C. Angelberger, O. Colin, P. Domingo, Combust. Flame 155 (2008) 247-266.

[33] F. Rebosio, A. Widenhorn, B. Noll, M. Aigner, Proc. ASME Turbo Expo 2010, GT2010-22751.

[34] E. Tangermann, M. Pfitzner, M. Konle, T. Sattelmayer, Combust. Sci. Techol. 182 (2010) 505–516.

[35] G. Kuenne, A. Ketelheun, J. Janicka, Combust. Flame 158 (2011) 1750-1767.

[36] V. Moureau, P. Domingo, L. Vervish, Combust. Flame 158 (2011) 1340-1357.

[37] B. Franzelli, E. Riber, L.Y.M. Gicquel, T. Poinsot, Combust. Flame 159 (2012) 621-637.

[38] G. Bulat, Large Eddy Simulations of Reacting Swirling Flows in an Industrial Burner, PhD thesis, Imperial College London, 2012.

[39] S. Wang, V. Yangs, G. Hsiao, S.Y. Hsieh, H. Mongia, J. Fluid Mech. 583 (2007) 99-122.

[40] P. Wolf, G. Staffelbach, A. Roux, L. Gicquel, T. Poinsot, V. Moureau, C. R. Mecanique 337 (2009) 385-394.

[41] P. Taylor, R. McMillan, D. Baker, Proc. ASME Turbo Expo 2000, 2000-GT-112.

[42] B.M. Igoe, SIEMENS technical paper, presented at Institute of Mechanical Engineers, Amsterdam, April 2008, URL: www.energy.siemens.com/hq/en/energy-topics/publications/technical-papers/gas-turbines.htm, downloaded on 18 July 2011.

[43] C. Engelbert, B. Göker, 16th International Energy & Environment Fair & Conference, Istanbul, May 2010, URL: www.energy.siemens.com/hq/en/energy-topics/publications/technical-papers/gas-turbines.htm, downloaded on April 2012.

[44] G. Bulat, D. Skipper, R. McMillan, K. Syed, Proc. ASME Turbo Expo 2007, GT2007-27266.

[45] E.R. Norster, S.M. de Pietro, DEUA Publication 495 (1996) 1-23.

[46] Scholz, M. H. H., de Pietro, S. M., International Gas Turbine & Aeroengine Congress & Exhibition, Orlando, Florida, June 1997, ASME paper 97-GT-61.

[47] M. Kowkabi, R. Noden, S. de Pietro, International Gas Turbine & Aeroengine Congress & Exhibition, Orlando, Florida, June 1997, ASME paper 97-GT-60.

[48] H. Al Kabie, R. McMillan, R. Noden, C. Morris, Proc. ASME Turbo Expo 2000, 2000-GT-111.

[49] R. McMillan, P. Martin, R. Noden, M. Welch, Power-Gen Europe, Barcelona, May 2004, URL: http://www.energy.siemens.com/hq/pool/hq/en energy-topics/pdfs/en/gas-turbines-power-plants/5_Gas_Fuel_Flexibility.pdf, downloaded on April 2012.

[50] Boyns, M. B., Patel, R., International Gas Turbine & Aeroengine Congress & Exhibition, Orlando, Florida, June 1997, ASME paper 97-GT-59.

[51] D.J. Cramb, R. McMillan, Proc. ASME Turbo Expo 2001, 2001-GT-0076.

[52] K.J. Syed, E. Buchanan, Proc. ASME Turbo Expo 2005, GT-2005-68070.

[53] K.J. Syed, K. Roden, P. Martin, J. Eng. Gas Turbines Power 129 (2007), 672-679.

[54] W.B. Ng, E. Clough, K.J. Syed, Y. Zhang, Meas. Sci. Technol. 15 (2004) 2303-2309.

[55] K.S. Chana, K.J. Syed, M.I. Wedlock, R.W. Copplestone, M.S. Cook, G. Bulat, Proc. ASME Turbo Expo 2005, GT-2005-68433.

[56] W.B. Ng, K.J. Syed, Y. Zhang, Exp. Thermal Fluid Sci. 29 (2005) 715-723.

[57] K.Y. Cheung, Y. Zhang, Meas. Sci. Technol. 17 (2006) 3221-3228.

[58] M. Wedlock, J.P. Wood, M.N. Miller, G.J. Sims, K. Liu, K. Syed, P. Bowen, A. Crayford, Y. Sevcevco, Proc. ASME Turbo Expo 2008, GT2008-50790.

[59] K. Liu, J.P. Wood, E. Buchanan, P. Martin, V.E. Sanderson, Proc. ASME Turbo Expo 2009, GT2009-59065.

[60] M.D. Turrell, P.J. Stopford, K.J. Syed, E. Buchanan, Proc. ASME Turbo Expo 2004, GT2004-

53112.

[61] A.C. Benim, M.P. Escudier, P.J. Stopford, E. Buchanan, K.J. Syed, Int. J. Fluid Mach. Sys. 1 (2008) 1-9.

[62] G. Bulat, P. Stopford, M. Turrell, D. Frach, E. Buchanan, M. Stöhr, Proc. ASME Turbo Expo 2009, GT-2009-59721.

[63] G. Bulat, W.P. Jones, A. Marquis, V. Sanderson, U. Stopper, 7th Mediterranean Combustion Symposium 2011.

[64] S.K. Sadasivuni, V. Sanderson, A. Bonaldo, G. Bulat, N. Swaminathan, 5th European Combustion Meeting 2011.

[65] U. Stopper, M. Aigner, H. Ax, U. Meier, R. Sadanandan, M. Stöhr, A. Bonaldo, Exp. Thermal Fluid Sci. 34 (2010) 396-403.

[66] U. Stopper, M. Aigner, W. Meier, R. Sadanandan, M. Stöhr, I.S. Kim, J. Eng. Gas Turbines Power 131 (2009) 021504.

[67] P.A. Strakey, M.J. Yip, J. Fluids Eng. 129 (2007) 942-953.

[68] H. Ax, P. Kutne, W. Meier, K. König, U. Maas, A. Class, M. Aigner, Appl. Phys. B 94 (2009) 705-714

[69] C. Morley: Gaseq, A Chemical Equilibrium Program for Windows, version 0.79, URL: www.gaseq.co.uk, downloaded on 29 November 2011.

[70] M.V. Heitor, J.H. Whitelaw, Combust. Flame 64 (1986) 1-32.

[71] J. Zhang, S. Nieh, Powder Technol. 112 (2000) 70-78.

[72] C. Cortés, A. Gil, Prog. Energy Comb. Sci. 33 (2007) 409-452.

[73] S.B. Pope, Turbulent Flows, Cambridge University Press, Cambridge, 2010, p. 281.

[74] R.W. Bilger, Proc. Combust. Inst. 22 (1988) 475-488.

[75] B. Böhm, J.H. Frank, A. Dreizler, Proc. Combust. Inst. 33 (2011), 1583-1590

[76] M.S. Sweeney, S. Hochgreb, M.J. Dunn, R.S. Barlow, Combust. Flame 159 (2012) 2912-2929

[77] U. Stopper, R. Lückerath, M. Aigner, B. Wegner, W. Krebs, in: VDI Wissensforum GmbH (Ed.), VDI-Berichte 2119, VDI Verlag, Düsseldorf, 201, p. 109-114.

[78] L.J. Spadaccini, M.B. Colket III, Prog. Energy Combust. Sci. 20 (1994) 431-460.

[79] J. Herzler, C. Naumann, Proc. Combust. Inst. 32 (2009) 213-220.

[80] P. Griebel, M. Witt, Numerische Untersuchung von laminaren Methan/Luft-Vormischflammen, report TM-50-00-07 at the Paul Scherrer Institut, Villingen, Switzerland, 2000, p. 15.

[81] N. Peters, Turbulent Combustion, Cambridge University Press, Cambridge, 2006, p. 78-79.

[82] T.R. Marrero, E.A. Mason, J. Phys. Chem. Ref. Data 1 (1972) 3-118.

[83] R. Borghi, in: C. Casci, C. Bruno (Eds.), Recent advances in aerospace sciences, Plenum Press, New York, 1985, p. 117-138.

[84] M. Tamura, P.A. Berg, J.E. Harrington, J. Luque, J.B. Jeffries, G.P. Smith, D.R. Crosley, Combust. Flame 114 (1998) 502-514.

[85] I.P. Herman, Optical diagnostics for thin film processing, Academic Press, San Diego, 1996.

[86] M.A. Gregor, F. Seffrin, F. Fuest, D. Geyer, A. Dreizler, Proc. Combust. Inst. 32 (2009) 1739-1746.